UNIVERSITAT DE BARCELONA

New technologies and their characterisation for nanostructured SnO_2 Gas sensor devices

Albert Cirera Hernández

Universitat de Barcelona

Departament d'Electrònica

New technologies and their characterisation for nanostructured SnO_2 gas sensor devices

Memòria de Tesi doctoral presentada per n'Albert Cirera Hernández per a optar al títol de Doctor en Física.

Barcelona, setembre de 2000.

5.1 Introduction

Whereas in the previous two chapters we focused in the development of new technologies for gas sensors devices and their characterisation, in this chapter we will pay attention to the physical phenomena involved on the sensors based on sputtered[1] layers. Thus this technology has shown high reliability from his issue few years ago and nowadays different companies are developing tin oxide based sensors obtained by sputtering (Motorola, MICS, Microsens).

In this way, the knowledge obtained from the study of powder based sensors is the background that will serve us to analyse the sputtered layers. The comparison of results will provide us a better understanding of the semiconductor gas sensor scope.

To obtain this knowledge and considering previous technological advances, we will focus on the study of the technological parameters having more incidence on the electrical performances of the sensors. So, samples have been selected to study sputtering target, the thickness of the layer and the annealing temperature.

Finally, the proved improvement of the sensors response after proper catalysation, is analysed by means of the study of different strategies for the addition of noble metal catalytic.

[1] In the following, to avoid misunderstanding, we will refer *sputter* for the deposition technology also known as *cathodic pulverisation*. *Ion-gun* or *bombarded* is kept for the removal process usually done in XPS measurements with Ar^+ ions. Nevertheless both process are based on the same physical process known as sputter. The use of specific software –Multipak, see appendix 1- with defined axis labels as those showed in section 5.2, suggest us to clarify this point.

5.2 Microstructure evolution of sputtered η-SnO_2

As we will expose in this section, similar study to powder samples has been performed. In fact, most of the presented sputtering-sample results on XRD and XPS show a close relation with those of powder samples. Therefore, similar phenomena of oxygen vacancy density could be expected. Nevertheless, the different morphology of the samples besides to different technological parameters introduces new conditions in the model.

Set	1	2	3
Target composition	SnO_2	Sn	Sn
Atmosphere in sputter chamber	70%Ar+30%O_2	100%O_2	100%O_2
Catalysation	No	No	Posterior Pd flash

Table 5.1. Samples studied in this section.

For the present study, two sputter targets were considered, tin and tin oxide ones. In order to known the influence of the catalytic, a posterior sputter flash was implemented in samples deposited by means of a tin target. These first technological differences allow us to distinguish 3 sets of samples –as seen in table 5.1-. All the samples were annealed in the range from 400 to 900°C in synthetic air during 8 hours.

According to preliminary works [Gutiérrez,99][Olaizola,99a][Olaizola,99b], 600 nm thick layer sensor showed acceptable performances as gas sensor. As we will show, the thickness induces a stress as consequence of the compactness of the layers, which is reduced when the thickness of the layer is also reduced. This reduction enhances the sensing properties, namely response time and sensitivity. Experimental details are given in the third chapter (3.2 Technology for sputter deposition).

5.2.1 XRD characterisation

As seen in the diffractograms, figure 5.1, sputtering samples follows similar evolution to liquid pyrolisis ones. All diffractograms show cassiterite SnO_2 structure. In the case of set 3, no Pd form (Pd metallic, PdO nor PdO_2) [JCPDS,97] is distinguished within the resolution of the XRD (~5%). In spite of these similarities, differences in the temperature at which diffractograms exhibit sharper reflections appear. As it can be observed, at temperature of 500/600°C samples exhibit similar degree of crystallinity than 700/800°C liquid pyrolisis ones.

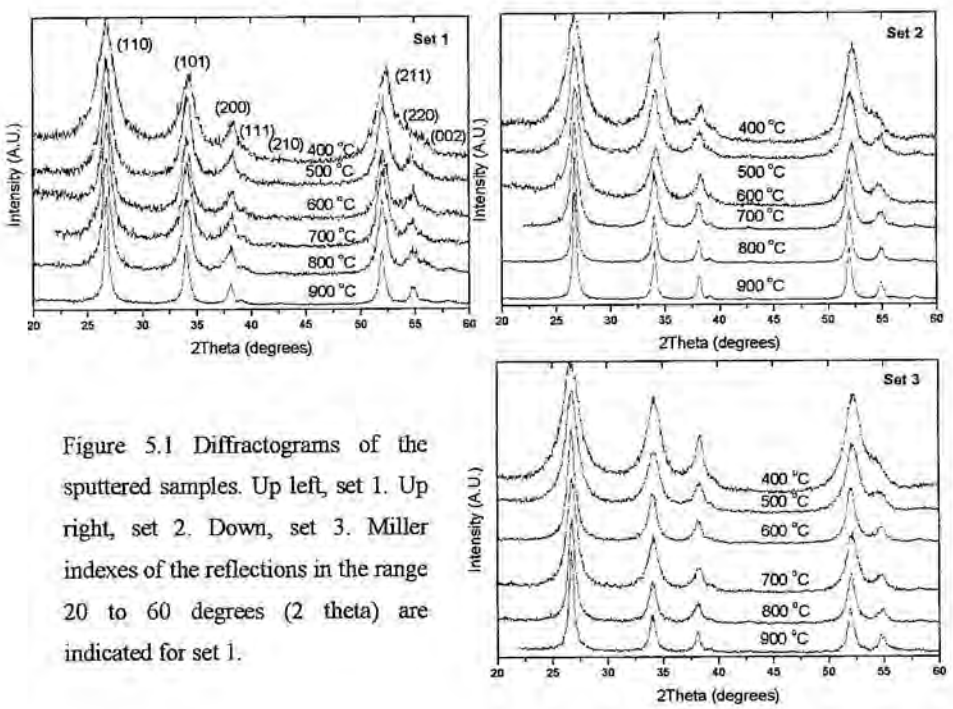

Figure 5.1 Diffractograms of the sputtered samples. Up left, set 1. Up right, set 2. Down, set 3. Miller indexes of the reflections in the range 20 to 60 degrees (2 theta) are indicated for set 1.

Besides, it is worth to observe how even in higher temperature samples (900°C), (111) and (210) reflection –in both cases h+k+l=odd, see equation (4.7) and further consequences- almost does not appear.

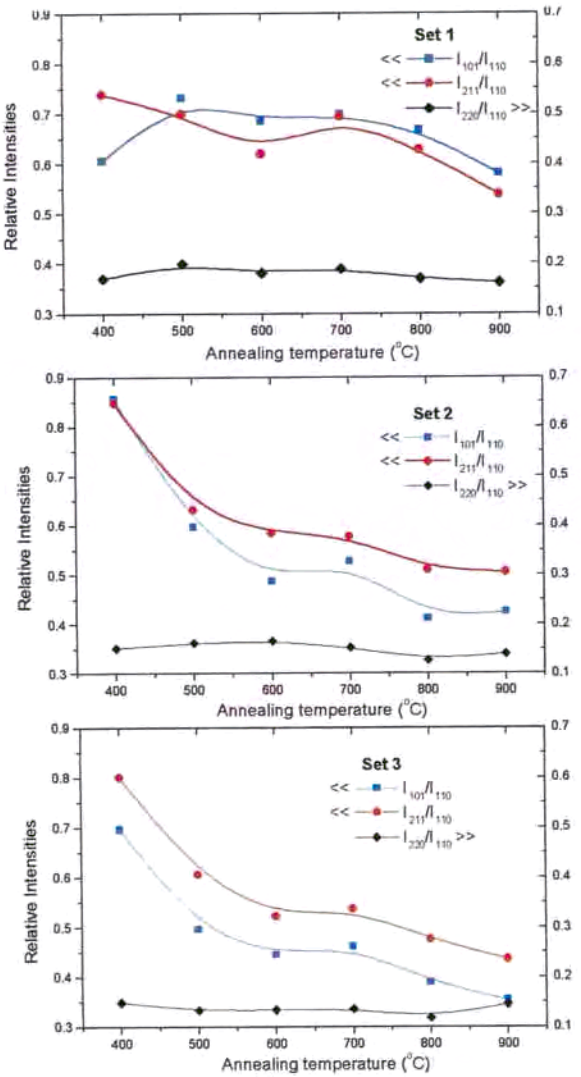

Figure 5.2. Relative intensities. From up to bottom, set 1, 2 and 3.

In order to analyse further differences between the three sets of samples, we will proceed calculating parameters with physical meaning –relative intensities, distortions, strain, and grain size-. As the intensity of some reflections becomes very difficult to fit at some annealing temperatures, we will focus on those planes that give information enough and become able to fit in all temperatures. Thus, systematic study is given for (110), (101), (211) and (220) atomic planes. References to other planes are given only when needed for special discussion.

5.2.1.1 Relative intensities

First, relative intensities are evaluated. As seen in figure 5.2, differences appear between set 1, by one side, and set 2 and 3 by the other. While in set 1 there is still no changes in relative intensities, set 2 and 3 exhibit an evolution more similar to such evolution shown in former chapter. Thus, for set 2 and 3, reflections (101) and (211) become less intense with higher stabilisation temperature with respect (110) and (220), which relative intensity is nearly constant.

As close angle between two adjacent reflections allows underrating differences between temperature factor, let me plot (211)/(220) relative intensity –see figure 5.3.

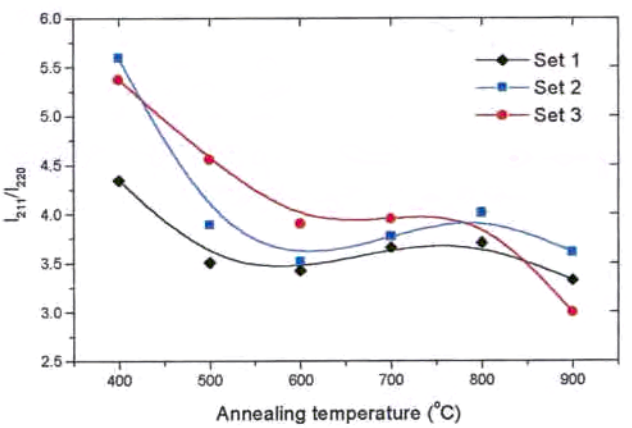

Figure 5.3. Relative intensities I_{211}/I_{220} versus annealing temperature.

In spite of all three sets exhibit a decrease of such relative intensity, set 2 and 3 exhibit a higher decrease than set 1.

5.2.1.2 Distortions

Following similar arguments than those developed for powder samples in previous chapter, distortions are computed considering differences between planes (110) and (220). Results are shown in figure 5.4.

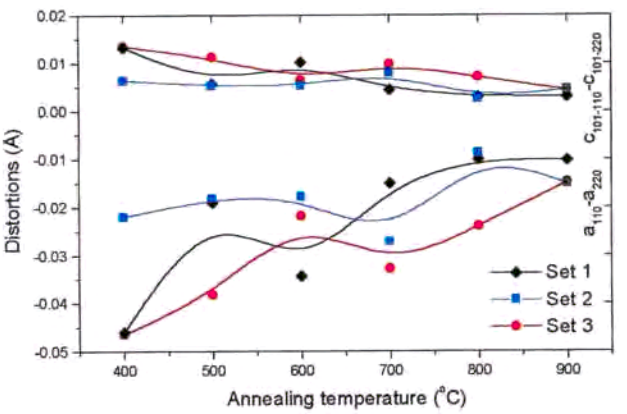

Figure 5.4. Distortions for the different sets of sputtered samples versus annealing temperature.

In spite of similar evolution to powder samples reducing distortions when annealing, an important difference appears because higher annealing does not reduce distortions. These remaining distortions are present in all the sets of samples, nevertheless some differences appear between sets.

5.2.1.3 Strain

Further knowledge on the thermal evolution of the microstructure of sputtered samples is achieved by computation of the strain, that is the deviation of atomic position with respect its relaxed position.

For this, one can compute the distance between planes by means of Bragg formula,

$$2d_{hkl}\sin\theta_{hkl} = n\lambda \qquad (5.1)$$

where d_{hkl} is the distance between planes with (hkl) Miller indexes, θ_{hkl} the angle of the reflection, n the order of the reflection and λ the wavelength of X-rays (see appendix 1).

In table 5.2, the distances between studied atomic planes of samples annealed at higher temperature are given together with other samples from references.

Reflection	$d_{hkl}^{900°C}$ (Å) Set 1	$d_{hkl}^{900°C}$ (Å) Set 2	$d_{hkl}^{900°C}$ (Å) Set 3	$d_{hkl}^{1000°C}$ (Å) [Yu,97]	d_{hkl} (Å) [JCPDS,97]
(110)	3.337	3.340	3.338	3.351	3.347
(101)	2.634	2.636	2.634	2.637	2.643
(211)	1.760	1.761	1.760	1.762	1.764
(220)	1.674	1.673	1.674	1.672	1.675

Table 5.2. Distance between atomic planes calculated by means of the Bragg formula applied to different reflections.

As it can be observed, some discrepancies mainly appear on the distance between (110) planes. The evaluation of this strain can be computed as the deviation of the distance between plains with respect the distance in a relaxed scenario:

$$\left\langle e^2 \right\rangle_{hkl}^{\frac{1}{2}}(T) \propto \frac{d_{hkl}^{relaxed} - d_{hkl}^{T}}{d_{hkl}^{relaxed}} \tag{5.2}$$

where d_{hkl}^{T} represents the position (obtained by means of Bragg formula) of the plane with Miller indexes (hkl) of sample processed at a temperature T. This formula allows computing the mean strain of the atoms in plane (hkl) in the normal direction to this plane.

For a first calculation, let me take the proportionality constant in equation 5.2 as 100 and the relaxed length as that indicated in reference [Yu,97] –table 5.2-.

As seen in table 5.3, (110) is highly strained even after high temperature annealing. This fact should be directly associated with the result obtained in the computation of the distortions. In that case the differential calculation of lattice parameters with planes (110) and (220) leads to an evaluation of the effects of strain – unrelaxed in plane (110) compared with (220)- on the lattice parameters.

Reflection	$\langle e^2 \rangle_{hkl}^{\frac{1}{2}}$ (900° C)	$\langle e^2 \rangle_{hkl}^{\frac{1}{2}}$ (900° C)	$\langle e^2 \rangle_{hkl}^{\frac{1}{2}}$ (900° C)
	Set 1	**Set 2**	**Set 3**
(110)	0.425	0.352	0.392
(101)	0.114	0.031	0.114
(211)	0.142	0.085	0.165
(220)	-0.100	-0.072	-0.127

Table 5.3. Strain calculated by means of equation 5.2 for the samples annealed at higher temperature. The relaxed distance between atomic planes given in [Yu,97] –table 5.2- are considered for computations.

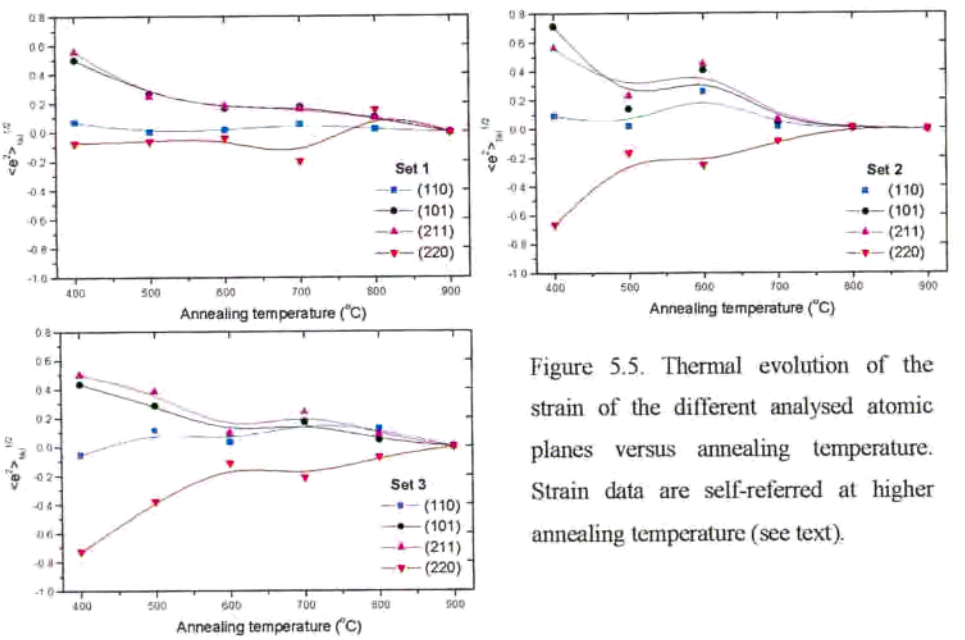

Figure 5.5. Thermal evolution of the strain of the different analysed atomic planes versus annealing temperature. Strain data are self-referred at higher annealing temperature (see text).

For a study of the actual evolution of the strain with the annealing temperature, it is useful take $d_{hkl}^{900°C}$ as the relaxed distance, since in spite of the residual strain present at this temperature, the evolution is better visualised. Therefore, the results

presented in figure 5.5 are not the actual strains, but are related with the strain evolution with the annealing temperature.

As seen, the behaviour of samples 2 and 3 exhibit some correspondence with that of powder samples analysed in previous chapter. In the case of set 1 difference consists on the non-tensile strain for (220). Other planes exhibit a very similar behaviour for all the sets; while (101) and (211) planes undergo compressive stress, (110) plane is still relaxed.

5.2.1.4 Grain size

We conclude the analysis of XRD spectra with the computation of grain size by means of Scherrer formula [Bartram,67]. As this computations is mainly related with the width and intensity of reflections, the actual interpretation of the physic origin of the results is confusing. Thus, a plane where lattice imperfections

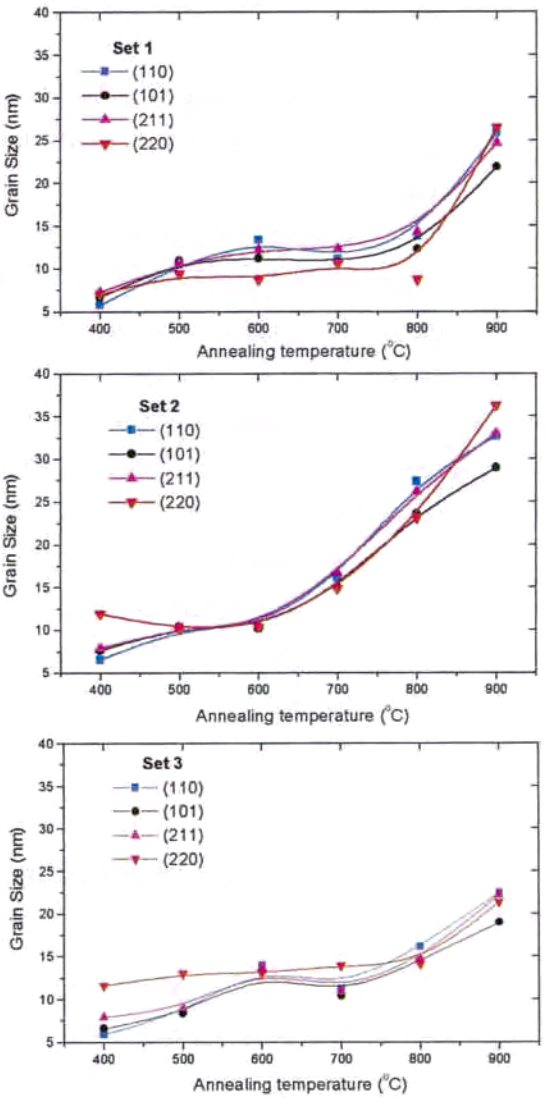

Figure 5.6. Grain size computed by Scherrer formula versus annealing temperature.

were present would exhibit a wider reflection, therefore smaller grain size would be measured. For this reason we analyse all the studied planes in figure 5.6.

As all the planes give similar results, we can assume that not great differences with the actual grain size should be present, being the results of the three sets comparable.

The initial value of all the sets becomes similar. An initial grain size of 6 nm when annealing at 400°C is obtained. This data is usual for lightly samples [Diéguez,96] [Cabot,00].

All the three sets show a light growth of particle size until 10-15 nm when annealing temperature is increased until 600°C. In fact, it has been widely reported how the grain size suddenly increases from 450°C [Yu,97][Barsan,00][Cabot,00], but this fact is not observed in these samples.

The evolution of grain size from 600°C until 800°C seems to be hindered for sets 1 and 3. It is worth to observe how the 800°C-annealed samples of both sets still reach 15 nm, while in set 2 sample is 25 nm large.

At temperature higher than 800°C, the hindering phenomenon is reduced and the grain continues its growth.

Besides these facts, it is worth to observe how in set 2 and 3, the grain size corresponding to low temperatures annealing is higher than in the other planes.

5.2.2 XPS characterisation

Complementary information to that obtained by bulk XRD inspection is performed by X-Ray Photoelectron Spectroscopy (XPS). As XPS is based on the photoelectric effect and the penetration length of the x-ray is low, we will consider that XPS data gives information of a 20 Å external shell of the nanograin.

The first data consists on the no contamination observed within the detection limit of XPS (~0.1%).

As seen in figure 5.7, spectra shows a shift of the binding energies towards lower energies when increasing the temperature.

It is interesting to observe a double state for oxygen, as it can be seen in figure 5.8.

Higher energy state of O1s band (noted in figure 5.8 as O'', with respect the bigger state O') could be associated to a chemisorbed carbon compound. While its relative area is considerable for non-bombarded samples, when ion gun is applied, its relative area is strongly reduced. In sample annealed at 500°C, this contribution vanishes since when cleaning with ion gun, carbon signal almost disappear (C1s<0.7%). This fact makes difficult to place the right energy zero.

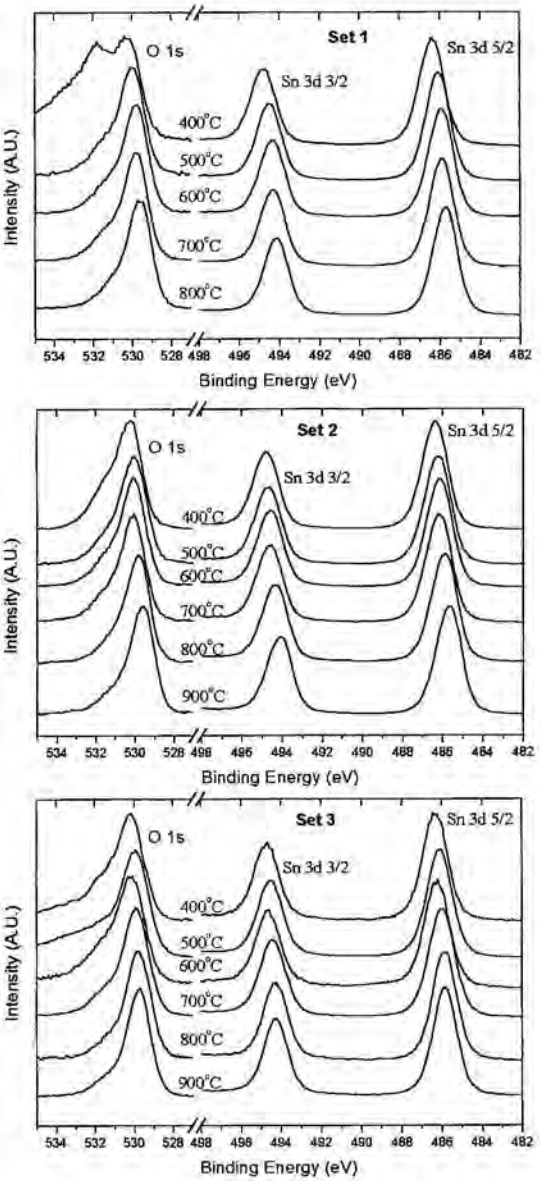

Figure 5.7. XPS spectra of the three sets of samples. Only peaks corresponding to tin and oxygen atomic orbitals are given.

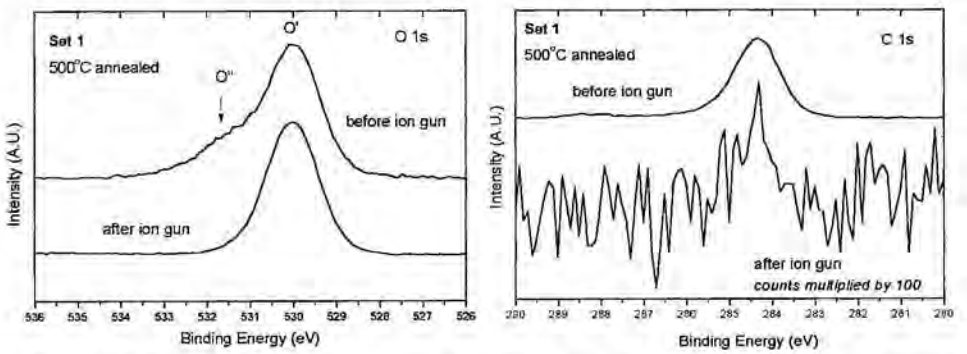

Figure 5.8. XPS spectra of the oxygen and carbon peak before and after ion gun for sample annealed at 500°C of set 1.Similar results can be observed in other samples.

But if association of O'' state with carbon is valid, as we took the C1s as reference orbital for right shift of the Fermi level (see Annex 1) considering full electric contact between C1s and SnO_2, the O''-state, related with carbon, should not follow the shifts of the tin and oxygen, unless the carbon compound be related with the cassiterite structure. To verify this sentence, we have plotted in figure 5.9 the binding energies of states O'' as function of binding energy of states O'.

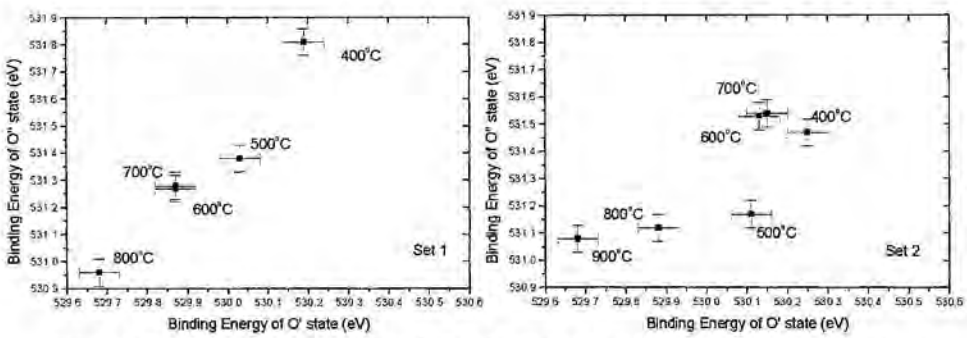

Figure 5.9. Binding energies of states O'' as function of binding energy of states O' for set 1 and 2. Annealing temperature is indicated by every binding energy.

The results are not very clear. But it seems to be a relation between the shifts of O' and O'', therefore these last cannot be uniquely associated to a carbon state. Other possibilities consist on chemisorbed species (such as O_2 or NO_2) or a different state of oxidation in tin oxide.

Regarding the peak width, this is a convolution of the natural line width (related with lifetime of the hole –or more generally, positive induced charge- resulting from the photoionization process), the natural width of the x-ray line which created the photoelectron line (0.9 eV, see annex 1) and the instrumental contribution to the observed line width [Moulder,92]. As the last two effects are considered similar for all the samples, a variation of the width should be related with the lifetime of the holes. Considering the uncertainty principle of Heisemberg ($\Delta E \Delta t \sim h$), as lower is the lifetime of the holes in the material, wider is the line width. It is well known that the photoelectron lines of insulating solids are of the order of 0.5 eV wider than photoelectron lines of conductors.

As seen in figure 5.10, before ion gun, line width decreases with the annealing temperature; this can be generally read as a reduction of the forbidden gap levels, able to recombine holes and reduce their lifetime. After ion gun, the FWHM lowers below data of before ion gun. But as shown in by Cabot *et al* [Cabot,00a], ion gun introduce tremendous number of states in the band gap. Therefore the contradictory can be only explained in the way of previous work

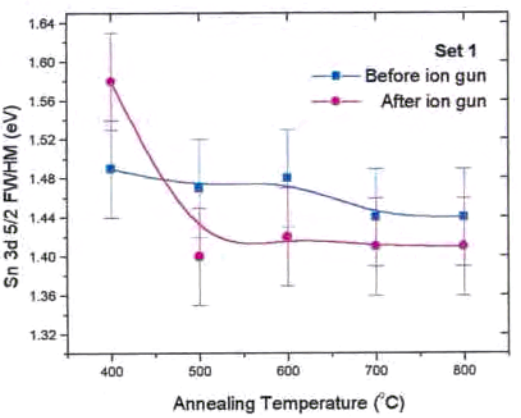

Figure 5.10. FWHM of the Sn 3d 5/2 orbital corresponding peak before and after ion gun versus annealing temperature for samples of Set 1. Similar results are obtained for other sets of samples.

[Kövér,95] that ensures the ion gun preferentially affects to oxygen atom, reducing the sample and producing local metallic states.

It is interesting to point out that FWHM of O'' state is higher than O', nevertheless both decrease with annealing temperature. While in the case of O' state (that is the O1s orbital coupled to tin) it can be understood, its interpretation for the O'' state (related with carbon) becomes more difficult.

The surface characteristic of XPS makes very difficult to assess the actual stoichiometry in SnO_x. Some works indicated that XPS measurements cannot give the actual stoichiometry [Cabot,00b][Diéguez,99].

Besides, the different surface reconstructions that tin oxide can undergo with the annealing

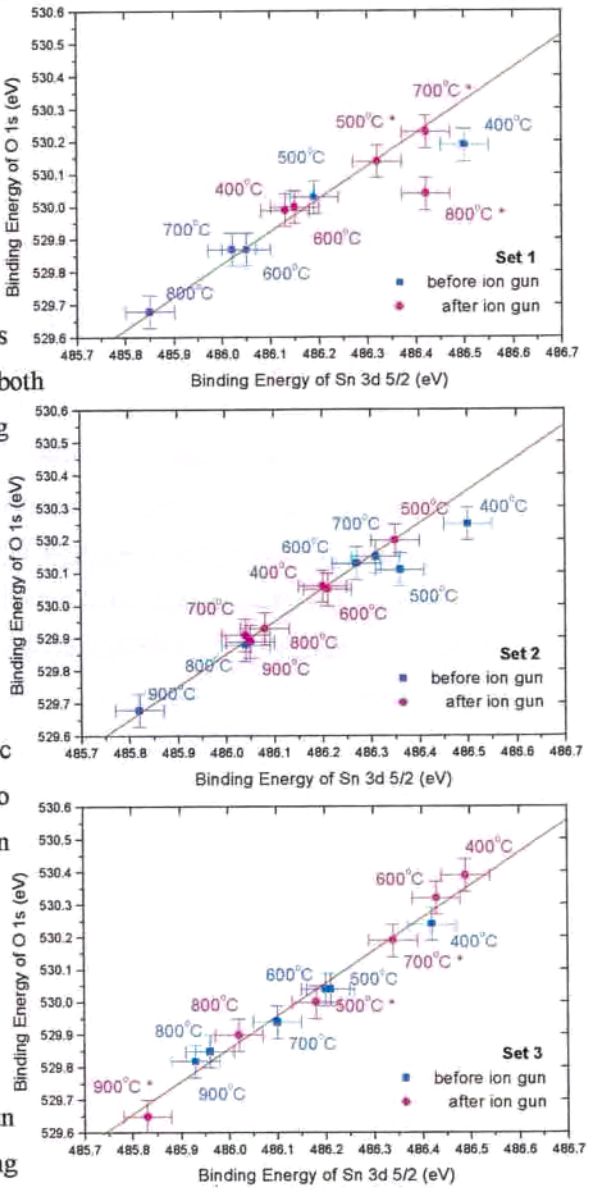

Figure 5.11. Binding energies of 1s oxygen orbital (O') as function of binding energy of Sn 3d 5/2 orbital for set 1, 2, and 3. Measurements are done before and after ion gun. In this last case, the star by the experimental data indicates uncertainty in the carbon shifting due to the low signal of this element. Annealing temperature is indicated by every binding energy. A straight line with slope 1 is drawn to verify how different samples follow the same relative shift.

temperature could give a higher signal than the bulk stoichimetry. Other effects such as the chemisorbed oxygen, the oxygen related with chemisorbed carbon and the oxygen related with additive species could also give signal.

Therefore, further information inferred from XPS should take into account other quantities with physical meaning, such as binding energies and a deep study of valence bands.

5.2.2.1 Tin and oxygen binding energy evolution

Since orbitals are coupled in a common electronic structure, tin and oxygen bands follow the same relative shifts.

The three sets of samples shows a shift towards lower energies when annealing temperature is increased, being similar the range of shift, about 0.7 eV. Both tin and oxygen orbitals follow similar variations within the experimental error.

When ion gun is applied, the correlation of the annealing temperature with the binding energy is lost.

The similar evolution of set 2 to set 1 indicate that the physic phenomena involved on binding energy evolution should be the similar, nevertheless it is worth observe small differences between set 1 and 2, that is samples of set 1 seems to exhibit a shift towards lower energies.

5.2.2.2 Analysis of Palladium catalyst in tin oxide.

Palladium exhibits a complex behaviour to be analysed by XPS. The main valence states of the atom are 0, 2 and 4, which binding energies are summarised in table 5.4.

State	Pd^0	Pd^{2+}	Pd^{4+}
Associated chemical compound	Pd metallic	PdO	PdO_2
Binding Energy (eV)	334.9-335.4	336.1-336.5	337.7-338.2
Relative Energy (eV)		1.2	1.3

Table 5.4. Binding energies of the Pd states, after [Wagner,78].

But before start fittings, let us pay attention to higher energy Pd state that appears in samples before ion gun. As only tin, oxygen and palladium –together with surface carbon- are present in our samples, this state is not very well understood; moreover it disappear when the Ar^+ ion gun is applied, as seen in figure 5.12.

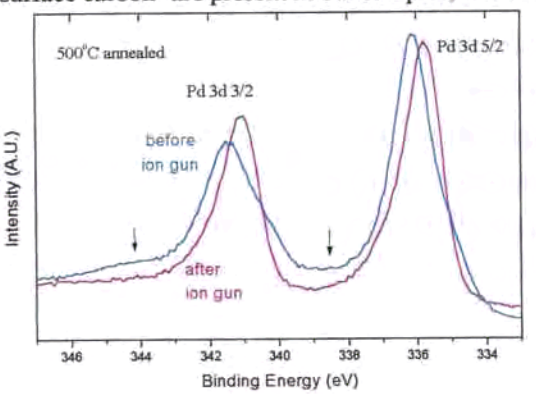

Figure 5.12. XPS spectrum of Pd 3d doublet of sample processed at 500°C before and after sputtering. The arrows indicate the higher energy states.

In spite we could conclude that the existence of such state would be related with a surface chemisorbed specie, it seems chemically difficult a chemisorption involving a chemical state 4+ due to the higher energy involved in such state. Therefore, for the calculation of the predominant chemical state, we will proceed with samples Ar^+ bombarded. For the calculations of the amount of palladium at surface, we will keep not bombarded measurements.

Some of the spectra clearly show the existence of three states in palladium, as shown in figure 5.13. Despite these states oscillate within the range of binding energies for Pd^0, Pd^{2+} and Pd^{4+}, they always keep the relative energies indicated in table 5.4, as well the relative intensities and energies between both spin states in the doublet.

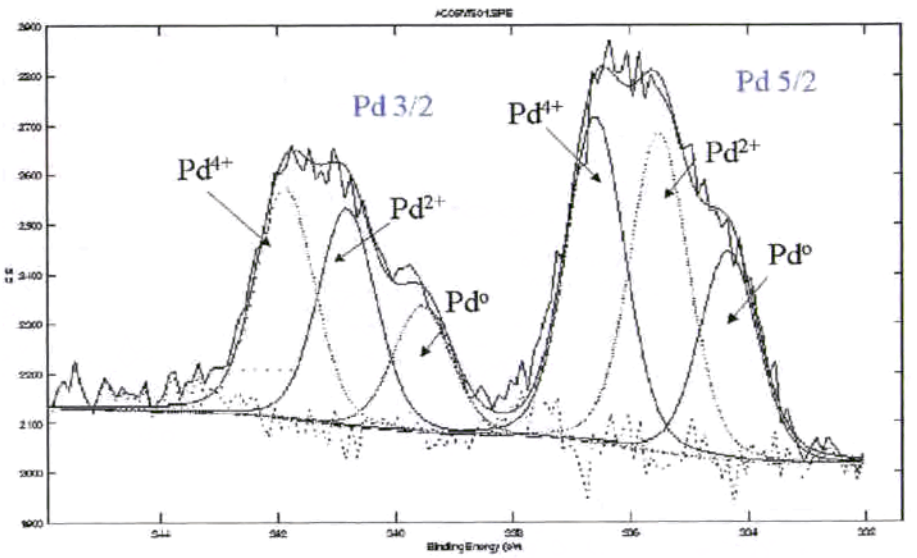

Figure 5.13. Example of fitting of the Pd doublet region in XPS spectrum for sample annealed at 800°C.

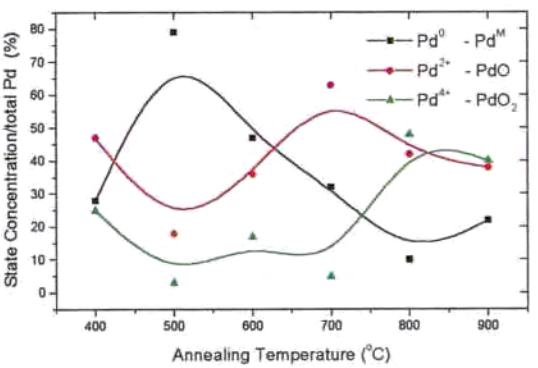

Regarding these considerations, the assessment of the actual state by means of XPS fitting becomes quite complex. In figure 5.14 is shown the evolution of such chemical states with the annealing temperature.

Figure 5.14. Relative atomic concentration of the different states of Pd (Pd^0,Pd^{2+} and Pd^{4+}) as function of the annealing temperature.

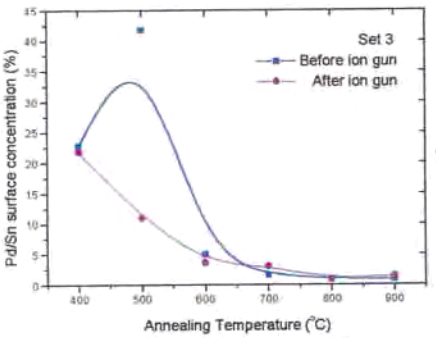

Figure 5.15. Palladium surface concentration with respect tin as function of the annealing temperature.

These data indicate a decrease of the Pd^0 state with the annealing temperature together with an increase of the ionised states (Pd^{2+} and Pd^{4+}). As no other compounds than O, C and Sn are present in the non-bombarded sputtered layers, the chemical identification of the states leads to Pd^0-Pd^M (metallic form), Pd^{2+}-PdO and Pd^{4+}-PdO_2.

It is interesting to study the ration Pd/Sn at the surface as function of the annealing temperature. As shown in figure

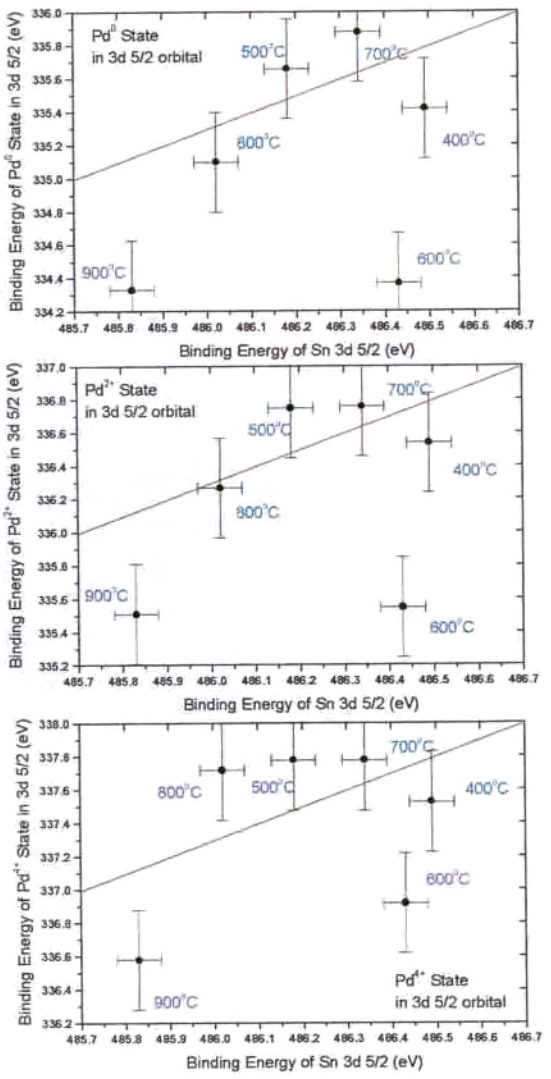

Figure 5.16. Binding energies of Pd^0, Pd^{2+}, and Pd^{4+} states in 3d 5/2 orbital as function of binding energy of Sn 3d 5/2 orbital

5.15, the amount of palladium mainly decreases from 20% to 2% before 600°C. Both diffusion towards the layer and evaporation of the noble metal can lead to this behaviour.

The study of the binding energy reveals that palladium states are not coupled to the tin oxide electronic bands, see figure 5.16.

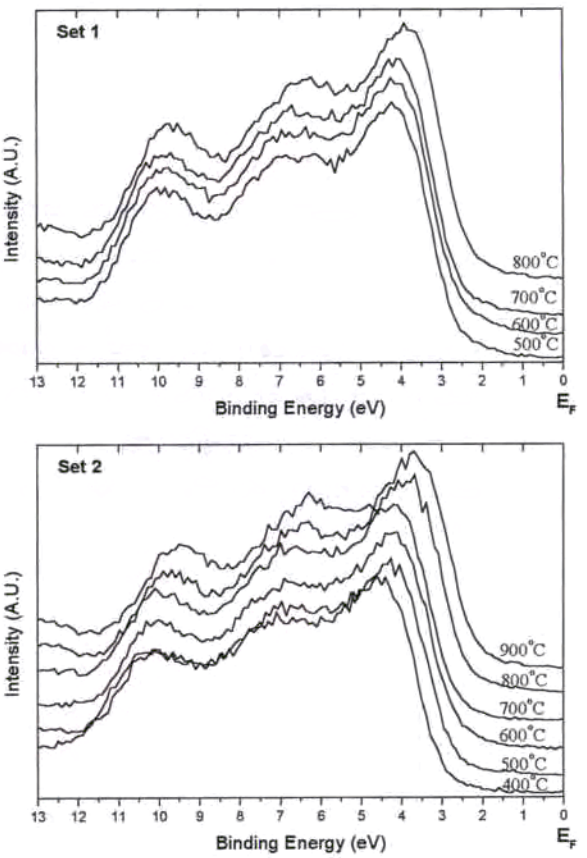

Figure 5.17. Valence bands of the XPS spectra of sets 1 and 2.

5.2.2.3 Valence bands

Finally the valence bands are analysed. In figure 5.17 are presented the valence bands for sets 1 and 2. The obtained spectra of the valence band can be considered as oxidised tin oxide [Cox,88] and surface reduced forms, such as SnO or Sn, should be discarded.

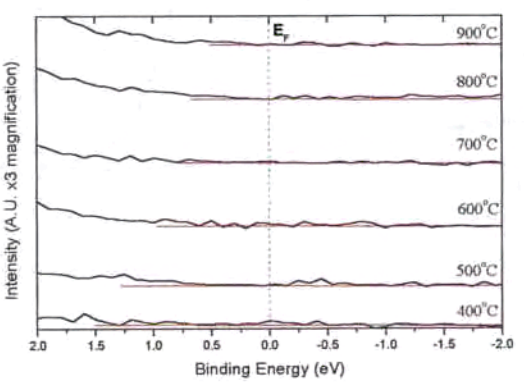

Figure 5.18. States near the Fermi level for set 2. Similar results are found for set 1.

As it can be seen in the figure, the top of the valence band exhibits a shift with the annealing temperature very similar to that followed by O 1s and Sn 3d 5/2 shown in figure 5.7.

In figure 5.18, the plot of bands near the Fermi level, shows the non existence of states laying by this level.

Considering the theoretical calculations for this band proposed previously [Kövér,95] –see figure 2.10- we have fitted our experimental spectra. As seen in figure 5.19, the tails of the O2p orbital –the most important in the surface tin oxide electronic structure [Munnix,83]- have been simulated by means of two additional symmetric peaks. Therefore the resulting system contains 6 peaks and the numerical stability of them makes the difficult fitting. In spite of such uncertainty in the fitting, obtained parameters related with O2p and main O2p tail are credible.

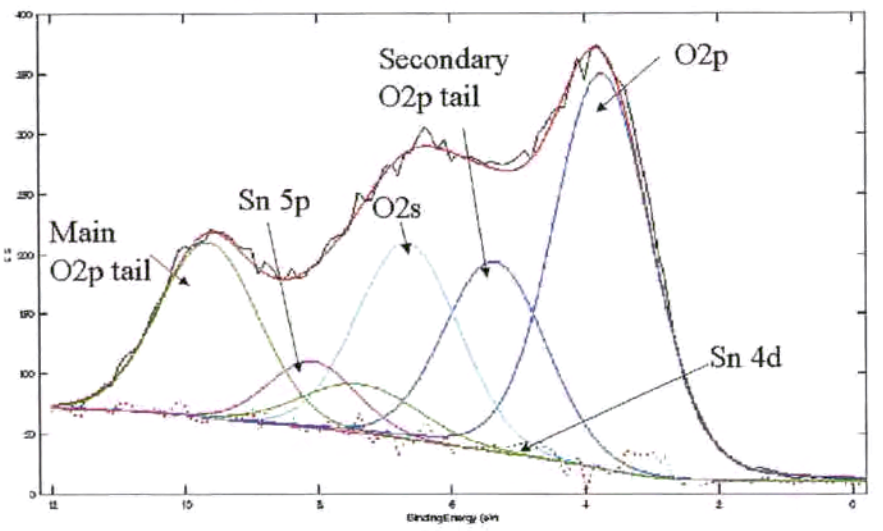

Figure 5.19. Example of fitting of the Valence Band. 6 peaks are needed for a reliable fitting, see text for more details.

As shown in figure 5.20, the first result of this fitting indicates a correlation of the Valence Band Maximum (the orbital O 2p) with the orbital Sn 3d 5/2 orbital and, considering figure 5.11, with the orbital O 1s.

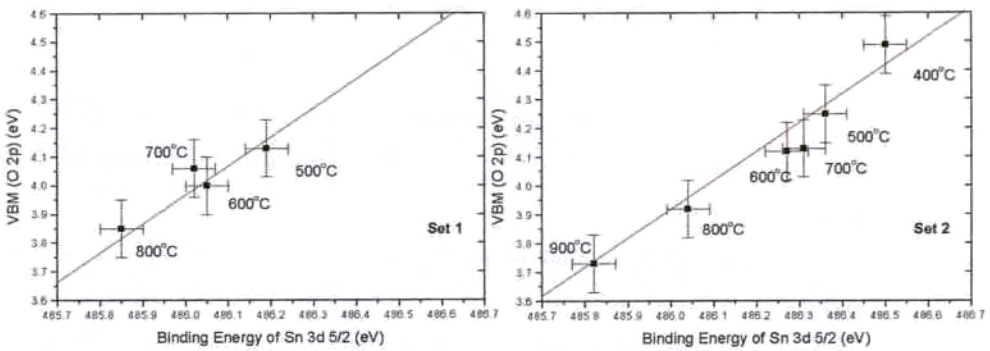

Figure 5.20. Binding energy of Valence Band Maximum (orbital O 2p) as function of binding energy of Sn 3d 5/2 orbital.

This figure shows a full agreement between the shift towards low energies of the valence band and the rest of electronic structure. This data becomes fundamental since outermost electrons of tin and specially oxygen are related with the valence band.

5.2.3 Discussion

Specific differences between set 1 (SnO_2 target), set 2 (Sn target) and set 3 (Sn target + Pd sputter flash) appear, but keeping a common structural evolution with the annealing temperature. These data suggest the existence of common physic phenomena involved in the evolution but conditioned by the sample origin and/or environment (i.e. sputter

target and additives). Therefore we will try to discuss the analysed data in order to distinguish common phenomena and specific differences.

5.2.3.1 A strained microstructure

Under our view the most comparable result arises from the analysis of strain. As shown in table 5.2, 900°C samples are strained, but the strain mainly affects in (110) plane.

In spite of the amount of atomic planes studied are not so large to conclude an exclusive effect on this plane, it is well known that (110) terminating surfaces are the most energetically stable due to thermodynamic arguments [Theil,76][Semancik,90] [Goniakowski,96] and therefore the predominant crystal face in policrystalline samples [Jarzebski,76]. But this consideration leads to an external origin (out of the nanocrystal) of the strain; inner origin should be rejected before.

The different origin (sputter target) and catalysation of the samples leading to the exposed evolution together with dry clean room technology makes difficult to consider any kind of contamination inside the grain as common origin.

Other kind of structural effect, such as crystallographic defects, can be also considered. Once exposed the model of oxygen vacancy evolution in powder samples, it seems very difficult that oxygen vacancies could explain residual strain after thermal treatments of 900°C during 8h in flowing synthetic air. It should be taken into account that at this temperature the recombination between atmospheric oxygen and oxygen vacancies even in bulk is very effective [Yu,97].

With respect the hypothesis of interstitial tin in tin oxide cassiterite lattice and relaxation effects, we have to take as reference the results of Agashe *et al* [Agashe,91]. In this work the author shows the relation of such defect with an anomalous increase of

the (200) intensity. As shown in the figure 5.1, our diffractograms do not present this anomalous behaviour and consequently we can discard this effect.

As the exposed inner phenomena becomes the most plausible, an external source of strain should be taken into account. In this case, it is necessary to consider a source of stress, which induces this strain. Once deposited, the mismatch between tin oxide and silicon oxide insulting substrate becomes the first possible source of stress. Nevertheless, to transfer this stress from the SnO_2/SiO_2 interface to the second and subsequent layers of nanoparticles seems physically impossible, attending the bulk measurement of strain performed by means of XRD.

As no satisfactory phenomenon is yet find, let me introduce the hypothesis of a relative high degree of compactness in order to explain the remaining strain at higher temperatures.

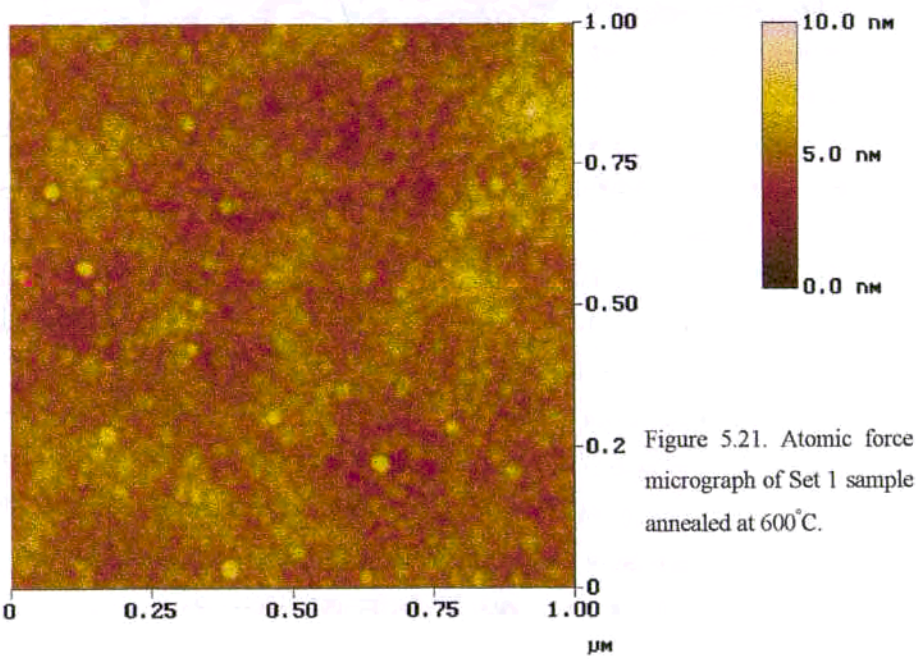

Figure 5.21. Atomic force micrograph of Set 1 sample annealed at 600°C.

First one can consider microstructure differences between powders and sputtered layers. While in powders samples grains can be in contact but keeping some non-contact surface [Diéguez,96], the continuous addition of tin (or tin plus oxygen) during SnO_2 formation leads to a more compact structure, as observed in [Wöllenstein,99].

In fact, the continuous addition growth in sputtering apparently does not seem the most appropriate way to obtain nanoparticles. In some cases sputtering is used to obtain even epitaxial layers of tin oxide [Semancik,91].

As a compact scenario could not give good results for sensing applications, the scientific community has applied different strategies. A reduction of the thickness of the layer increases the sensitivity of the device [Sberveglieri,92b], what could be understood as a reduction in the addition process of tin on tin oxide. Further works tried to exploit this way obtaining 3 layers of nanograins with a thickness of 80 nm each one [Sangaletti,97].

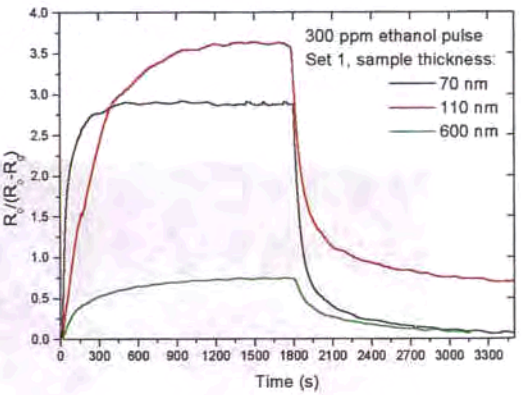

Figure 5.22. Sensitivities to 300 ppm of ethanol at 500°C in dry air for different thickness (70, 110 and 600 nm) of Set 1 sensors.

If such thickness is not achieved, SnO_2 particles can growth until 1-2 μm [Sberveglieri,92b][Aste,94] leading to high response times up to 10 minutes for 1000 ppm of ethanol [Aste,94]. In some cases thin films (~100 nm) leads to highly agglomerated SnO_2 but with low grain size (<10 nm) [Wöllenstein,99]. In this situation the response of the sensor can spend even hours to monitor 100 ppm of CO or 3 ppm of NO_2 if the sensing material is not properly catalysed.

A surface inspection of the matter structure by means of AFM is shown in figure 5.21. As seen in the figure, the sample is agglomerated but with a uniform grain size distribution.

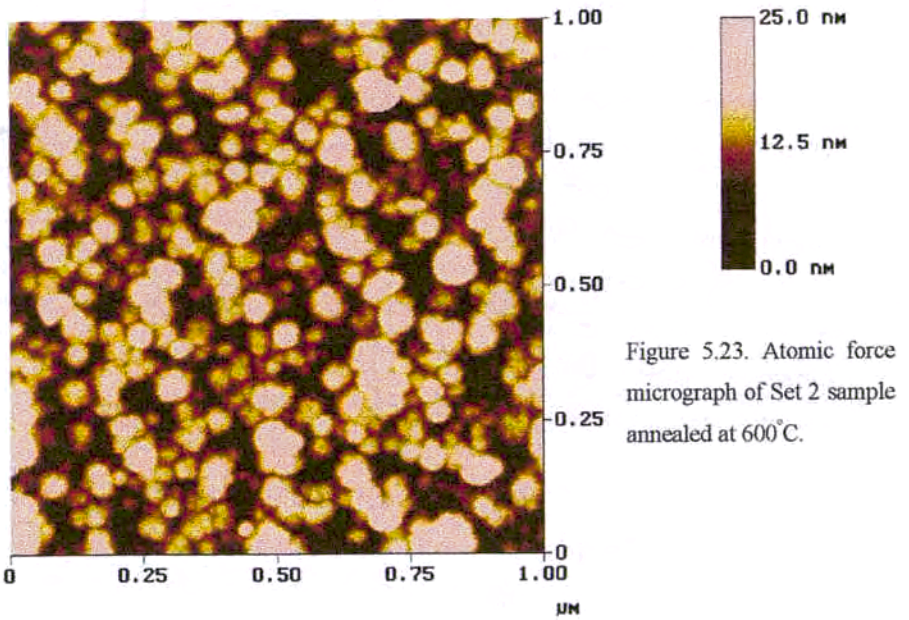

Figure 5.23. Atomic force micrograph of Set 2 sample annealed at 600°C.

In order to verify the previous hypothesis, the sensor response was investigated as function of the thickness –see figure 5.22-.

As seen, the sample 600 nm-thick shows relative low sensitivity and high response time (~10 min). When the thickness is decreased, both sensitivity and response time enhance, even reaching this last parameter about 2 min. These results could be understood as an enhancement of the porosity by means of thickness reduction.

With respect these effects on set 2, strain values are lower than in set 1 (table 5.3). Figure 5.23 shows less compactness at the surface.

Electrical results on these samples indicate better sensitivities and response times even for thicker samples (600 nm), as shown in figure 5.24.

200 nm-thick samples of set 2 shows sensitivity variations even for low concentration of CO (100 ppm).

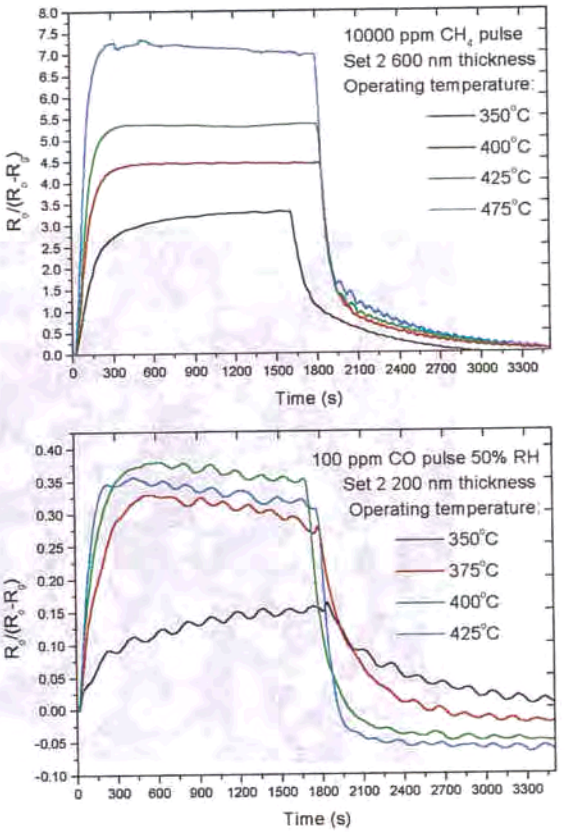

Figure 5.24. Up, sensitivities to 10000 ppm of CH_4 at different operating temperatures in dry air for a 600 nm-thick set 2 sample. Down, sensitivities to 100 ppm CO in 50% RH air of a 200 nm thick set 2 sample.

5.2.3.2 Competitive effects on the microstructure evolution

As we have exposed, most part of the microstructural evolution is related with the stress induced by compactness. However our results on powder samples indicate that other effects –mainly the presence of oxygen vacancies- have to be also considered when studying the microstructural evolution.

In this way, two main surprising thermal evolutions have been observed: the evolution of the relative intensities I_{211}/I_{220} (figure 5.3) as well as the binding energy evolution presented in figure 5.11.

In this case two differences are present with respect powder samples:

- ✓ Annealing times is much higher (8h) in comparison with that powder samples undergo (about 0.5 h).
- ✓ A stress arises from higher compactness inducing a strain that remains even after high temperature annealing.

Under the hypothesis of oxygen vacancy diminution with the annealing temperature, the first point should induce an advance of the process, leading to a diminution of the oxygen vacancies at lower temperatures, as effectively observed on sputtered samples.

Regarding the second point, compactness should difficult the oxygen diffusion in the sample and inside the nanograins. Therefore a delay of this effect is expected.

Consequently, annealing timing and deposited structure (compactness) play a competitive role in the microstructure of the sample.

If the effects of oxygen vacancy evolution are compared with those presented in previous chapter –mainly relative intensity (fig. 5.3), distortions (fig. 5.4) and strain (fig. 5.5)-, it can be deduced that the main recombination of oxygen vacancies are present before 500/600°C. Despite the main variation takes place before this temperature, after it we can observe lighter variations. As example, strain in set 2 and 3 for (220) plane are mainly reduced before 500°C (fig. 5.5), but its reduction extends until 800/900°C.

This data can be compared with those obtained by Yu *et al* [Yu,97], who shows the effects attributed to a wide diminution of oxygen vacancies at 400°C for powder samples annealed during 6h. In this case, no more variations are observed in samples after this temperature. Therefore, the comparison with powder samples leads to hypothesis that the soft evolution after transition temperature (500/600°C) is related with sputtered structure of the samples, and especially with the compactness.

Attending specific differences between samples, the hypothesis of a competitive effect between the compactness and the oxygen vacancy evolution, it is

worth to observe how some structural parameters indicate less influence of the oxygen vacancy evolution in set 1 samples. As seen in figure 5.3, the evolution of the relative intensity I_{211}/I_{220} is small compared with that sets 2 and 3 undergo. Besides, while (220) strain shown by sets 2 and 3 are comparable with that shown for powder samples, in the case of set 1, this is nearly zero. Figure 5.25 schematises the main features of the proposed differences between samples 2 and 3.

Once reached a satisfactory explanation for the bulk effects based on a competitive effect between compactness and oxygen vacancy diminution, surface effects, those measured by XPS, should be analysed.

Concerning valence band measurements, none of the presented phenomena induces appreciable surface states between the Fermi level and the valence band (fig. 5.17 and 5.18) nor appreciable influence on the valence band fittings (fig 5.19 and 5.20). This result could be associated with that obtained numerically by Munnix *et al* [Munnix,86][Munnix,87], who found that different vacancy configurations on (110) surfaces do not introduce a bound state in the gap. This result has been experimentally supported [Kohl,92][Rantala,94].

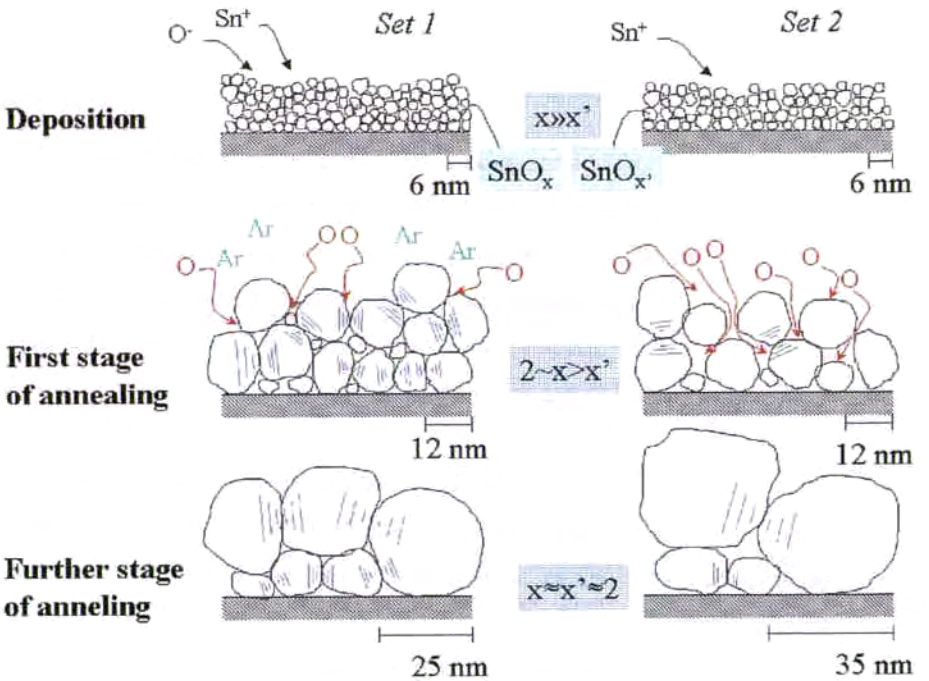

Figure 5.25. Scheme of microstructure evolution for Set 1 and 2. The deposition leads more oxidised tin oxide in set 1 than set 2. First stage of annealing induces higher compactness in set 1 than 2 and, therefore, better oxygen recombination in the set 2. Finally the compactness hinders the grain growth in set 1.

A more complex understanding is required when analysed the binding energy evolution. As annealing temperature induces a shift towards lower binding energy, different phenomena can be taken into account:

- ✓ A reduction with the annealing temperature of single and double ionised oxygen vacancies donor levels. As this levels lies at 30 and 150 meV of the conduction band [Fonstad,71], it is expected a shift of the Fermi level towards conduction band when they are filled of carriers. As shown, the

vacancy concentration decreases with temperature and, therefore, the Fermi level moves towards valence bands, leading to lower binding energies.

- ✓ A surface arrangement able to reduce the concentration of surface defects and, therefore, able to reduce the surface band bending that SnO_2 usually exhibits. This bending is mainly due to defects that involve ionic charge. As these defects are thermodynamically unstable, annealing temperature should reduce its concentration and flats the bending. Therefore a decrease of the binding temperature is expected.

As wide description of these phenomena was done in previous chapter, we won't give more details. Besides, it was exposed that in order to distinguish both phenomena it is necessary to perform very fine experiments, and we do not have the subsequent data.

Despite of this leak of further analysis, let us pay attention to the wide variety of samples that undergo this binding energy variation:

- ✓ Sol-Gel pure samples and ex-situ catalysed (Pd, Pt, Au) [Diéguez,99]
- ✓ Sol-Gel samples in-situ catalysed (Pd, Pt, Au) [Cabot,00]
- ✓ Liquid-pyrolisis pure and in-situ catalysed samples –previous chapter-.
- ✓ Microwave pure and in-situ catalysed samples –previous chapter-.
- ✓ Sputtered tin oxide target highly agglomerated pure samples –this chapter-.
- ✓ Sputtered tin target less agglomerated pure samples –this chapter-.
- ✓ Sputtered tin target Pd catalysed samples –this chapter-.

Under our view, all these samples exhibit similar bulk properties at low annealing temperature –that is, the oxygen defective tin oxide structure-, but the variety of the samples is a variety of surface scenarios.

Therefore, despite we cannot experimentally conclude about oxygen vacancy diminution (bulk effect) or band bending flattening (surface effect), our view is the wide variety of different surface and interface kinds of samples which undergone binding energy variation discard the hypothesis of surface flattening.

5.2.3.3 The effects of palladium on microstructure

Once understood the main phenomena involving the sputter target, the thickness and the annealing temperature on samples, it is necessary to pay attention to the effects of catalysation.

Obviously set 3 (Pd catalysed) should be compared with set 2 (pure tin oxide) since both are obtained form the same kind of sputter target (Sn). Let me proceed in the same way we have developed this discussion.

Regarding high annealing temperature strain (table 5.3), set 3 exhibits higher strain than set 2. In spite of similar evolution with the annealing temperature (fig 5.5) are followed by both sets, set 2 (pure) seems reach a stable value at about 700°C while set 3 (catalysed) do not reach.

It is interesting analysing this temperature to the Pd/Sn surface concentration at that temperature shown in figure 5.15. As shown in this figure, the surface concentration of palladium is strongly decreased at this temperature. Some experimental results allow to discard the Pd evaporation [Fryberger,89].

The easier hypothesis to explain these effects consist in a diffusion of the surface Pd towards the layer when temperature are over 600°C. This palladium would fill the intergrain spaces increasing the stress of the SnO_2 nanograins.

Despite this mechanical relation between Pd and SnO_2, the binding energy of the palladium does not seem to be coupled to tin one (fig 5.16). This fact has been

recently showed for powder samples for Pd^0 and Pd^{4+} states [Cabot,00b], nevertheless in that study Pd^{2+} is related with tin oxide structure.

5.3 Study of catalysation strategies in sputtered η-SnO_2

Once established the main features of the microstructre of the SnO_2 samples, to achieve reliable sensors is necessary to develop a system for proper catalysation of tin oxide. Nowadays palladium and platinum are both the main catalytics for the improvement of SnO_2 sensing performances [Torvela,91][Lee,89][Fryberger,90][Klober,91]. Therefore their introduction is the main subject of study in this section.

Whereas in powder SnO_2 a wide variety of catalyst introduction procedures are used (impregnation [Diéguez,99], electroless [Sun,98], in-situ catalysation [Cabot,00a]) obtaining good sensing properties, in the case of sputtered layers the procedure becomes more difficult. As shown by Schweizer-Berberich *et al* [Schweizer-Berberich,96] the development of comparable sensors leads to better powder based sensors than sputtered ones.

5.3.1 Catalysation configurations

Despite the sensing mechanism involving catalycs are still not very well understood, it is accepted that a high concentration of catalyst Pd or Pt induces the combustion of reducing gases, such as CO and CH_4, reducing the sensitivity.

In order to achieve an homogeneous distribution of the catalyst in the sensing layer, not only surface Pd or Pt sputter flash is considered, but also buried layers of catalysts and combination of three buried layers. See scheme in figure 5.26

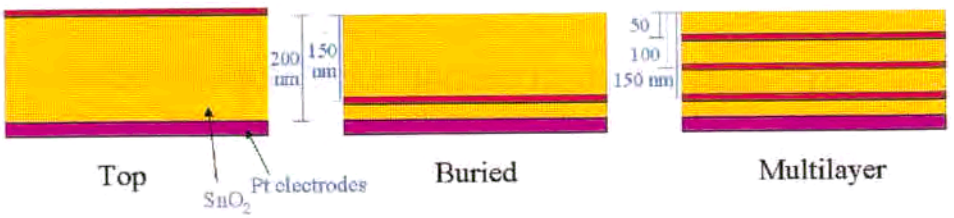

Figure 5.26. Scheme of the three studied catalysation strategies. Left, surface catalysation (*Top*). Centre, buried layer of catalyst (*Buried*). Combination of 3 catalyst buried layers (*Multilayer*).

As the structural study of the previous section, it has been shown that a reduction of the sensing layer thickness improves the sensitivity and response time, therefore 200-nm thick samples are used. Besides, lower residual strain of Sn-target sputtered samples makes the resulting material more appropriate for the usual SGS working conditions.

From the point of view of catalysation, DC-sputter flash of the noble metal additive at a pressure of $5 \cdot 10^{-3}$ mbar and intensity of 0.05 A during 90s are used. This sputter is believed to produce a thickness layer in the order of several equivalent monolayer.

In the first studied configuration (*Top*), the catalyst is placed by means of a sputter deposition after the tin oxide sputter growth.

A second configuration (*Buried*) consists on the deposition of the flash in a buried layer. To achieve this configuration, a first 50 nm-thick (nominal) layer of tin oxide is deposited, then the sputter flash is performed and the rest of the tin oxide (150 nm).

Finally, the third configuration (*multilayer*) consists on the deposition of three buried layers at 50, 100 and 150 nm (nominal) from surface.

For the study of such catalysation, XPS depth profiles were carried out on the samples. Ar^+ ion-gun was used to achieve the studied depth. As different ion-gun

intensities were used, there is no direct relation between sputter time (ion-gun time) and depth.

5.3.2 Top catalysation

Despite the use of 200-nm thick samples in this section, we studied those from set 3 in the present study in order to understand the influence of temperature on the palladium diffusion.

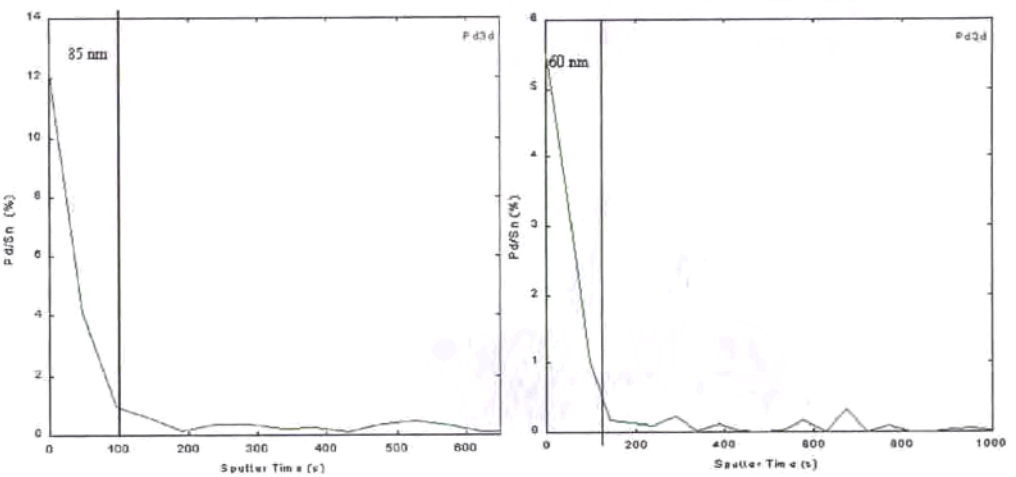

Figure 5.27. Pd/Sn profile of the Pd top catalysation of 400 (right) and 600°C (left) annealed samples. Left, atomic concentration of the whole profile.

As seen in figure 5.27 and 5.28, the diffusion of the Pd at temperature below 600°C are similar (within the experimental error), but at 800°C a wide diffusion of palladium is achieved. It is interesting to observe how the diffusion is related with a diminution of the Pd/Sn concentration.

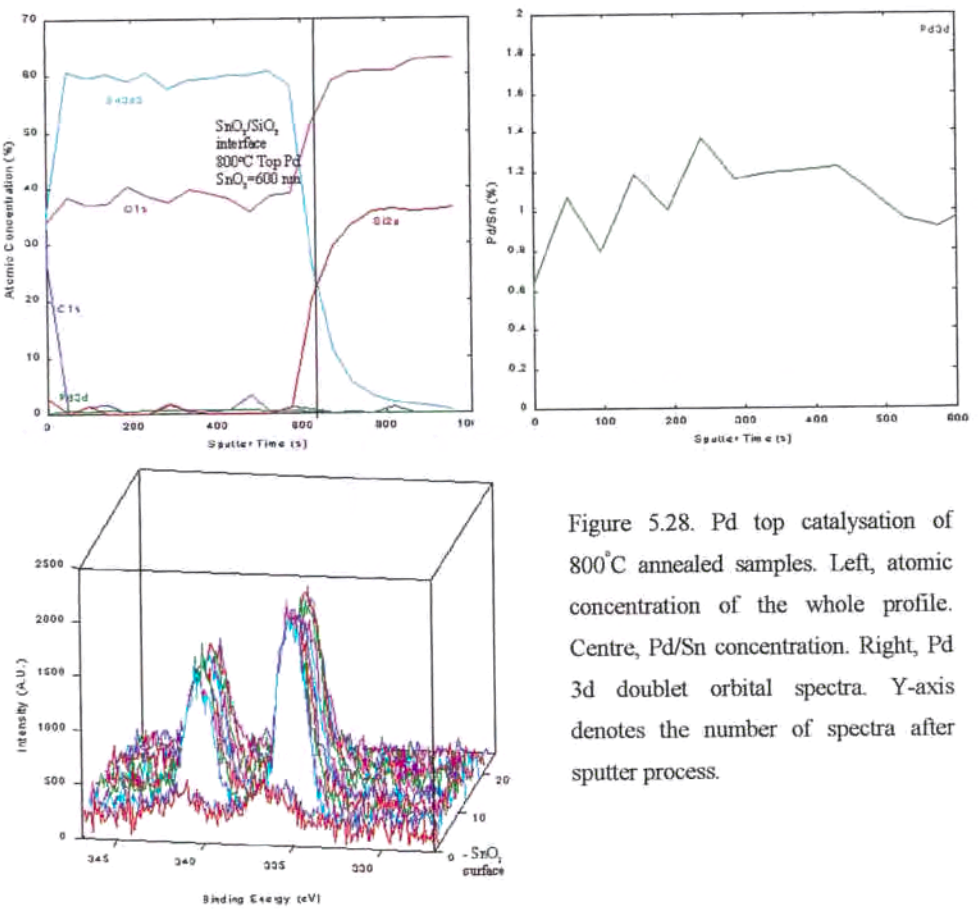

Figure 5.28. Pd top catalysation of 800°C annealed samples. Left, atomic concentration of the whole profile. Centre, Pd/Sn concentration. Right, Pd 3d doublet orbital spectra. Y-axis denotes the number of spectra after sputter process.

5.3.3 Buried catalysation

As observed in figure 5.29, the catalysation with a Pd buried layer implies the diffusion of the catalytic material through almost all the layer. This layer, nominally placed at 50 nm of the SnO_2/SiO_2 interface, extends until about 25 nm of the interface and reach the

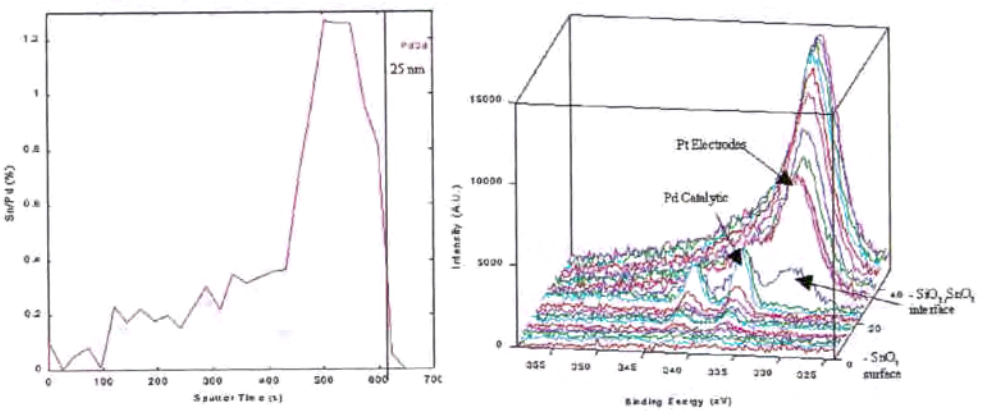

Figure 5.29. Left, Pd/Sn concentration profile of the Pd buried catalysed sample. Right, spectra profile showing the SnO_2/SiO_2 interface and platinum electrodes.

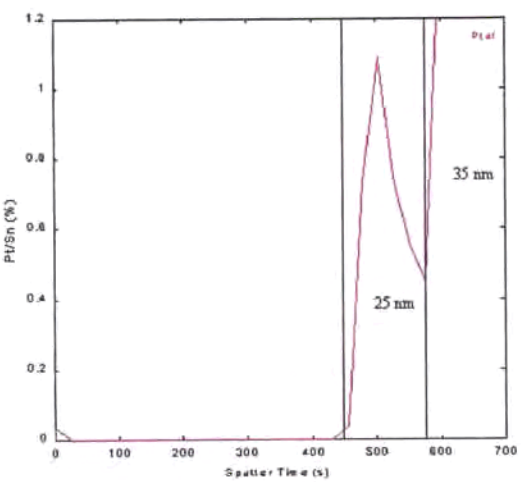

Figure 5.30. Pt/Sn concentration profile of the Pt buried catalysed sample

surface. The maximum concentration is about 1.2% Pd/Sn in a region 50 nm-thick.

These calculations become difficult since the presence of platinum of the electrodes for resistivity measurement placed at the interface.

Despite this wide diffusion of palladium, the platinum almost does not diffuse. As it can be seen in

figure 5.30, the diffusion keeps in a narrow area of about 25 nm. In this area the maximum concentration is about 1.1 % Pt/Sn, but strongly decreases out of this maximum. This implies that the actual concentration of platinum is notably less than palladium.

It is worth to observe the precision in the placement of the buried layer that in both cases are about 500 s of sputter time (identical sputter conditions in both samples).

5.3.4 Multilayer catalysation

In the case of multilayer deposition, a clear additive effect of the catalyst concentration is observed. Thus figure 5.31 shows the three deposited layers of palladium which concentration overlap increasing the maximum concentration of the single buried layer showed in the former subsection from 1.2 to 3 % Pd/Sn.

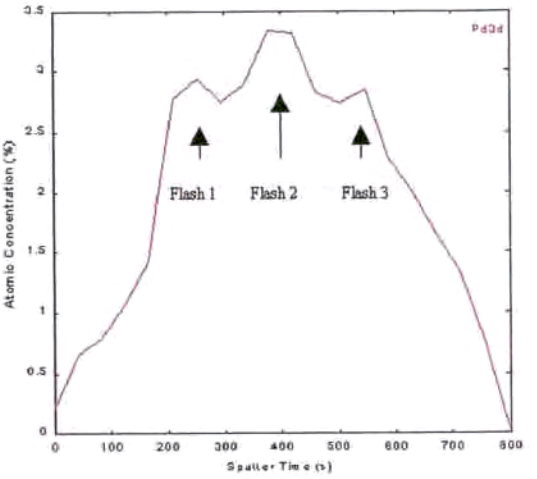

Figure 5.31. Pd/Sn concentration profile of the Pd multilayer catalysed sample.

In the case of platinum (figure 5.32) addition similar effects are observed but, as we showed in the previous subsection, the sharper concentration peaks are observed. Another difference of such sample is the segregation of platinum towards SnO_2. Both results can be understood considering that platinum forms big clusters as that shown in the figure 3.2. Therefore the areas where the amount of platinum is higher are the centre

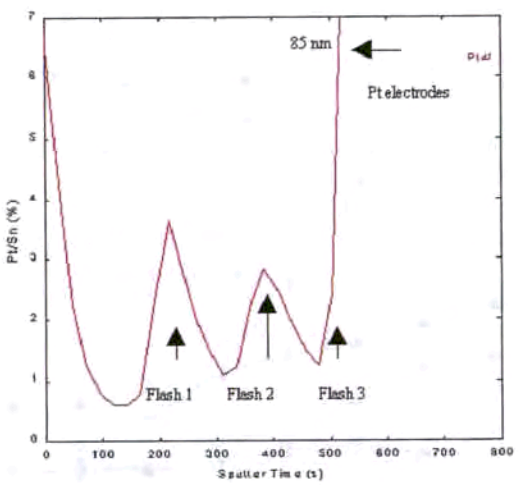

of such clusters which takes matter from areas with lower concentration. Besides, the platinum cluster formation is more probable in low stress environments such as surface.

Figure 5.32 Pt/Sn concentration profile of the Pt multilayer catalysed sample.

5.3.5 Electrical results.

As we have shown, considerable differences appear between the samples. As summary, it seems that top catalysation does not diffuse as inner catalysation. The multilayer leads to a direct addition of the catalyst concentration with respect the buried configuration. Besides, whereas palladium diffuses quite well inside the layer, platinum lays in narrower areas. This last result could be possibly related with the cluster formation of platinum.

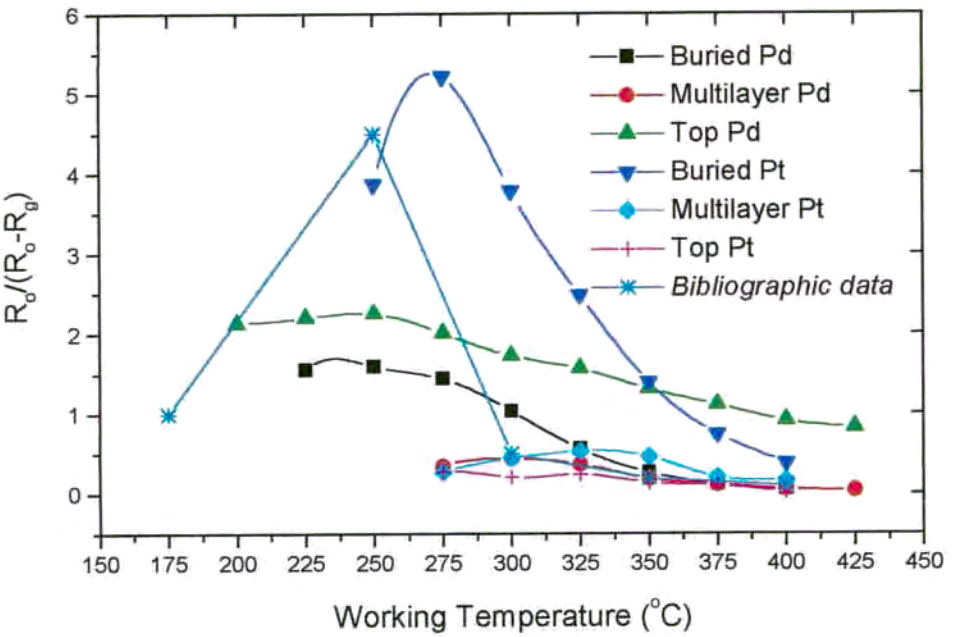

Figure 5.33. Sensitivity as function of the working temperature for 100 ppm exposure. Results of the studied strategies for catalysation are compared with those results showed in the work [Schweizer-Berberich,96] for thin film sensors catalysed with platinum.

The diffusion of the catalytic additive until the electrodes suggest thinking in an influence of these electrodes on the sensing phenomena, as it has been already studied [Fukui,93][Ylinampa,93].

Results on sensitivity –figure 5.33- shows how buried layer increases sensitivity at lower temperatures. In the case of top layers, only the palladium increases catalysation. At the contrary platinum and palladium multilayers becomes poor sensitives.

Despite the difficulty to know the actual sensing phenomena involving these results, some considerations can be done.

Previous work indicate that proper catalysation is achieved when sputtering platinum in quantities about 1-2 equivalent monolayers [Schweizer-Berberich,96]. Other

similar works indicated that less than 8 nm of surface catalytic (less than 60 s of sputter) leads to good sensors for H_2 sensing applications [Mizsei,93][Mizsei,95]. In general it is considered that higher quantities of catalytic could *kill* the sensing performances of the catalysed layer by means of a fast combustion of the proper gas.

These considerations about the excess of catalytic are supported by the results obtained by Galdikas *et al* [Galdikas,97] where XPS profiles of Pt buried layers show concentrations about 10 % of platinum being the resulting sensors quite poor in sensitivity –about 0.2- even for 500 ppm of CO.

In the case of multilayer catalysation, the effect of direct sum of catalyst concentration could lead to an excess of catalyst in the whole sensing layer. Therefore the sensors does not exhibit very high sensitivity to CO.

The case of surface catalysation is more complicate. While platinum tends to form clusters at surface, palladium easily diffuses towards the interior of the sensing layers. Thus it seems that the Pd addition by this configurations should be more effective than for platinum.

Finally the buried catalysation gives the best results. Despite the differences in the homogeneity of the catalysation between the studied layers and powders, the results obtained –about 1% - are in the order of magnitude of known good concentrations for powder technology.

5.4 Conclusions and critic review

In this chapter we have presented an applied characterisation for the improvement of sputtering technology. The main part of the work was focused on the knowledge of the main structural properties of the sputtered tin oxide. The main obtained conclusions were:

- ✓ As consequence of the layer morphology, the compactness of the layers induces a strain that remains even at higher temperatures annealing treatments. This strain is higher for SnO_2-target sputtered samples.
- ✓ The annealing temperature induce changes in the microstructure parameters–strain, distortions, relative intensities and binding energies- that are believed to be related with the diminution of oxygen vacancies with the annealing temperature.
- ✓ The compactness of the implemented layers is improved by a reduction of the thickness of such layers. This leads to better sensing properties, especially sensitivity and response time.
- ✓ The influence of surface palladium lightly modifies the microstructural behaviour of the samples. Palladium diffuses at temperatures higher than 600°C and is a light contribution to the strain of the layer.

The use of such knowledge helps to the development of SnO_2 layers with better performances, able to be catalysed. In this context, three different strategies of catalysation were tested. *Top*, *buried* and *multilayer* catalysation by means of platinum and palladium exhibit different properties:

- ✓ The surface catalysation (top) with palladium produces a diffusion of such metal through the layer. Good electrical results are obtained when palladium is used. In

the case of platinum the results are poorer as consequence of the cluster formation of such metal on surface.

- ✓ The catalysation with buried layers of both platinum and palladium gives good results. Especially those sensors catalysed with platinum exhibit changes of resistivity about 5 under exposures of 100 ppm of CO.
- ✓ Despite multilayer catalysed sensors exhibit changes of resistivity under gas exposure, their results are worst than previous catalyst configurations. This leak of catalytic performances is related with an excess of the noble metal additive, which concentration is widely increased by the successive catalysation.

In this field, the future work should consider an improvement of the microstructure, reaching even more porosity in the layers. For this improvement, it should be considered not only the reduction of the layer thickness, but the sputtering parameters, which probably would lead better results if the growth of the layer is moved out of the equilibrium.

Once reached this goal, a proper catalysation with multilayer additives in lower concentration should lead to sensors with even better sensing performances.

Finally a proper study on material and sensing properties will be needed to assess the actual performances of the obtained sensors. For this study, the main part of the presented characterisation can be a solid base for the knowledge of the material.

References

In chronological order

[Bartram,67] S. F. Bartram, "Crystallite-size determination from line broadening and spotty patterns", from "Handbook of X-Rays", Eds. E. J. Kaelble, McGraw-Hill, New York (1967).

[Fonstad,71] C.G. Fonstad, R.H. Rediker, "Electrical propierties of high-quality stannic oxide crystals" , J. Appl. Phys, 42 7 (1971) 2911-2918.

[Jarzebsky,76] Z.M. Jarzebski, J.P. Marton, "Physical properties of SnO_2 materials (I,II i III)", J. Electrochem. Soc. (1976) 199C.

[Theil,76] B. Theil, R. Heilbig, "Growth of SnO_2 single crystals by a vapour phase reaction method" J. Cryst. Growth 32 (1976) 259-264.

[Wagner,78] C.D. Wagner, W.M. Riggs, L.E. Davis, J.F. Moulder, G.E. Muilenberg, "Handbook of x-ray photoelectron spectroscopy", Perkin-Elmer Corporation, Eden Prairie (1979).

[Munnix,83] S. Munnix, M. Schmeits, "Electronic structure of tin dioxide surfaces", Physical Review B, 27 12 (1983) 7624-7635.

[Munnix,86] S. Munnix, M. Schmeits, "Electronic structure of point defects on oxide surfaces", Phys. Rev. B 33, 6, (1986) 4126-4144.

[Munnix,87] S. Munnix, M. Schmeits, "Electronic structure of oxygen vacancies on TiO_2 (110) and SnO_2 (110) surfaces", J. Vac. Sci. Technol. A, 5 (1987) 910-913.

[Cox,88] D.F. Cox, T.B. Fryberger, S. Semancik, "Oxygen vacancies and defect electronic states on the SnO_2 (110)-1x1 surface", Phys. Rev. B 38 3 (1988) 2072-2083.

[Fryberger,89] T.B. Fryberger, J.W. Erickson, S. Semancik, "Chemical and electronic properties of Pd/SnO_2 (110) model gas sensors", Surface and interface analysis, 14 (1989) 83-89.

[Lee,89] D.D. Lee, W.Y. Chung, "Gas-sensing characteristics of SnO_{2-x} thin film with added Pt fabricated by the dipping method", Sensors and Actuators, 20 (1989) 301-305.

[Fryberger,90] T.B. Fryberger, S. Semancik, "Conductance response of Pd/SnO_2(110) model gas sensors to H_2 and O_2" Sensors and Actuators, 20 (1990) 305-309.

[Semancik,90] S. Semancik, F.B. Fryberger, "Model studies of SnO_2 based gas sensors: vacancy deffects and Pd additive effects", Sensors and actuators B, 1 (1990) 97-102.

[Agashe,91] C. Agashe, M. G. Takwale, V. G. Bhide, S. Mahamuni, S. K. Kulkarni, "Effect of Sn incorporation on the growth mechanism of sprayerd SnO_2 films", J. Appl. Phys. 70 12 (1991) 7382-7386.

[Klober,91] J. Klober, M. Ludwig, H.A. Schneider, "Effect of thickness and additives on thin film SnO_2 gas sensors", Sensors and Actuators B, 3 (1991) 69-74.

[Semancik,91] S. Semancik, R.E. Cavicchi, "The growth of thin, epitaxial SnO_2 films for gas sensing applications", thin solid films, 206 (1991) 81-87.

[Torverla,91] H. Torvela, P. Romppainen, S. Leppävuori, "Reduction of the interference caused by NO and SO_2 in the CO response of Pd-catalysed SnO_2 combustion gas sensors", Sensors and Actuators B, 4 (1991) 479-484.

[Kohl,92] D. Kohl, "Oxidic semiconductor gas sensors", in *Gas Sensors*, G. Sberveglieri (ed.), Kluwer, Dordrecht, 1992.

[Moulder,92] J.F. Moulder, W. F. Stickle, P.E. Sobol, K.D. Bomben, "Handbook of x-ray photoelectron spectroscopy", Perkin-Elmer Corporation, Eden Prairie (1992).

[Sberveglieri,92a] G. Sberveglieri, "Classical and novel techniques for the preparation of SnO_2 thin-film gas sensors", Sensors and Actuators B, 6 (1992) 239-247.

[Sberveglieri,92b] G. Sberveglieri, G. Faglia, S. Groppelli, P. Nelli, "Methods for the preparation of NO, NO_2 and H_2 sensors based on tin oxide thin films, grown by

means of the r.f. magnetron sputtering technique", Sensors and Actuators B, 8 (1992) 79-88.

[Fukui,93] K. Fukui, M. Nakane, "Effects of tin oxide semiconductor-electrode interface on gas sensitivity characteristics", Sensors and Actuators B, 13-14 (1993) 589-590.

[Mizsei,93] J. Mizsei, "Activating technology of SnO_2 layers by metal particles from ultrathin metal films", Sensors and Actuators B, 15-16 (1993) 328-333.

[Ylinampa,93] A. Ylinampa, V. Lantto, S. Leppävuori, "Some differences between Au and Pt electrodes in SnO_2 thick-film gas sensors", Sensors and Actuators B, 13-14 (1993) 602-604.

[Aste,94] T. Aste, D. Beruto, R. Botter, C. Ciccarelli, M. Giordani, P. Pozzolini, "Microstructural development during the oxidation process in SnO_2 thin films for gas sensors", Sensors and Actuators B, 18-19 (1994) 637-641.

[Rantala,94] T.S. Rantala, V. Lantto, T.T. Rantala, "A cluster approach for the SnO_2 (110) face", Sensors and Actuators B, 18-19 (1994) 716-719.

[Kövér,95] L. Kövér, G. Moretti, Zs. Kovács, R. Sanjinés, I. Cserny, G. Margaritondo, J. Pálinkás, H. Adachi, "High resolution photoemission and Auger parameter studies of electronic structures of tin oxides", J. Vac. Sci. Technol. A, 13 3 (1995) 1382-1388.

[Mizsei,95] J. Mizsei, "H_2-induced surface and interface potentials on Pd-activated SnO_2 sensor films", Sensors and Actuators B 28 (1995) 129-133.

[Voschchilova,95] R.M. Voshchilova, D.P. Dimitrov, N.I. Dolotov, A.R. Kuz'min, A. V. Makhin, V.A. Moshnikov, Y. M. Tairov, "Forming the structure of gas-sensitive layers of tin dioxide produced by reactive magnetron sputtering", Semiconductors 29 11 (1995) 1036-1039.

[Diéguez,96] A. Diéguez, A. Romano-Rodríguez, J.R. Morante, U. Weimar, M.Schweizer-Berberich, W.Göpel, "Morphological analysis of nanocrystalline SnO_2 for gas sensors", Sensors and Actuators B 31 (1996) 1-8.

[Goniakowski,96] J. Goniakowski, M.J. Gillan, "The adsorption of H_2O on TiO_2 and SnO_2 (110) studied by first-principles calculations", Surface Science 350 (1996) 145-158.

[Schweizer-Berberich,96] M. Schweizer-Berberich, J.G. Zheng, U. Weimar, W. Göpel, N. Bârsan, E. Pentia and A. Tomescu, "The effect of Pt and Pd surface doping on the response of nanocrystalline tin dioxide gas sensors to CO", Sensors and Actuators B, 31 (1996) 71-75.

[Galdikas,97] A. Galdikas, S. Kačiulis, A. Mironas, A. Šetkus, "Gas induced resistance response in ultra-thin metal films covered with non-conductive layers", Sensors and Actuators B, 43 (1997) 186-192.

[JCPDS,97] JCPDS XRD card 41-1445 (SnO_2 Cassiterite synthetic). International Centre for Diffraction Data (1997). Further information can be found in McCarthhy, J. Powder Diffraction 4 (1989) 156.

[Sangaletti,97] L. Sangaletti, L.E. Depero, A. Diéguez, G. Marca, J.R. Morante, A. Romano-Rodriguez, G. Sberveglieri, "Microstructe and morphology of tin dioxide multilayer thin film gas sensors", Sensors and Actuators B, 44 (1997) 268-274.

[Yu,97] K.N. Yu, Y.Xiong, Y. Liu, C.Xiong, "Microestructural change of nano-SnO_2 grain assemblages with the annealing temperature", Physical Review B, 55, 4 (1997) 2666-2671.

[Horillo,98] M.C. Horillo, J. Getino, L. Arés, J.I. Robla, I. Sayago, F. J. Gutierrez, "Measruments of VOCs with a semiconductor electronic nose", Journal of Electrochemical Society, 145 7 (1998) 2486-2489.

[Shimizu,98] Y. Shimizu, T. Maekawa, Y. Nakamura, M. Egashira, "Effects of diffusivity and reactivity on sensing properties of thick film SnO_2-based sensors", Sensors and Actuators B 46 (1998) 163-168.

[Sun,98] R.D. Sun, D.A. Tryk, K. Hashimoto, A. Fujishima, "Formation of catalytic Pd on ZnO thin films for electroless metal deposition", J. Electrochem. Soc., 145 10 (1998) 3378-3382.

[Gutierrez,99] A.M. Gutierrez, J.A. Diez, S.M. Olaizola, E. Terrón, G. García, E. Castaño, F.J. Gracia, "Influence of the thin film thickness on the methane gas sensor selectivity", proceedings of Sensor'99 (1999) 171-175.

[Olaizola,99a] S.M. Olaizola, "Crecimiento de películas delgadas de SnO_2 mediante pulverización catódica para el desarrollo de microsensores de gas metano", PhD thesis at the University of Navarra (1999).

[Olaizola,99b] S.M. Olaizola, A. Cirera, G. García, A. Cornet, J.R. Morante, E. Castaño, F.J. Gracia, "Fabrication process of methane selective gas sensors", proceedings of CDE'99 (1999) 79-82.

[Diéguez,99] A. Diéguez, "Structural analysis for the improvement of SnO_2-based gas sensors", PhD thesis at the University of Barcelona (1999).

[Sauvan,99] M. Sauvan, C. Pijolat, "Selectivity improvement of SnO_2 films by superficial metallic films", Sensors and Actuators B, 58 (1999) 295-301.

[Wöllenstein,99] J. Wöllenstein, M. Jägle, P. Roetsch, H. Böttner, W.J. Becker, E. Wagner, "The influence of Pt-clusters at the surface of highly dense SnO_2 nano-films on the NO_2/CO sensitivity" Proceedings of Transducers 99 (1999).

[Barsan,00] N. Barsan, M. Schweizer-Berberich, W. Göpel, "Fundamental and practical aspects in the design of nanoscaled SnO_2 gas sensors: A status report", to be published in Sensors and Actuators B, (2000).

[Cabot,00a] A. Cabot, J. Arbiol, J. R. Morante, U. Weimar, N. Bârsan, W. Göpel, "Analysis of the noble metal catalytic additives introduced by impregnation of as obtained SnO_2 sol-gel nanocrystals for gas sensors", Sensors and Actuators B, accepted for publication.

[Cabot,00b] A. Cabot, "Additive effects on tin oxide nanopowders for gas sensing applications", Research thesis (*treball d'investigació de 3er cicle*) at the University of Barcelona (2000).

6. Conclusions, main findings and critic review

At the moment of the conclusion of this thesis, I realise of the good luck that has followed our work. Some of the ideas and experiments became innovative findings and developments, and their scientific and technologic value have been recognised. However, a small quantity of personal effort and moderate dose of imagination was necessary to develop the exposed work.

As introduced in the first chapter, the objective of this thesis is the development and implementation of classical and new technologies, in order to start SnO_2-based sensor laboratory production in our Department, and to carry it towards the paradigm of the transducer: sensitivity, selectivity, stability and smart consumption.

As first step of sensor production we have developed two new technologies for the production of nanocrystalline powder tin oxide: **liquid pyrolysis and microwave treatments**. Both technologies have been shown their suitability for gas sensing applications. Thus, stabilised nanoparticles are obtained and palladium or platinum catalysed material can be obtained by means of in-situ procedure; without the necessity of posterior treatments after the material obtaining.

Whereas in the case of microwave treatment, the amount of obtained tin oxide per batch is high, lower rate production is achieved by means of liquid pyrolysis.

The test measurements indicated the feasibility for gas sensing applications in both cases. However, the use of a higher ratio of Pd catalysation, until reaching active filter properties allowed a **CO-CH_4 selectivity improvement**.

The study of such catalysed material indicated that Pd coats tin oxide in 1 monolayer equivalent. Whereas the tin oxide keeps its structural properties, the coating is able to induce the CO burning producing CO_2.

Once developed the technologies for the tin oxide production, its characterisation according the **nanostructural evolution with the annealing temperature** has been performed in order to understand the structural properties of such material and to avoid structural drifts under working temperature.

In the case of nanopowders, the interpretation of the characterisation data indicates the diminution of oxygen vacancies with the annealing temperature. In order to compare technologies, sputtered tin oxide has been also studied by means of the same methodology, and the results indicated in this case a competitive effect between oxygen vacancy evolution and stress arising from the compactness of the layer.

In order to verify the reliability and feasibility of industrial implementation of the obtained nanopowders, these have been implemented on silicon micromachined substrates. Two new techniques were developed for such implementation, **pulverisation coating** and **microprinting**. Both technologies showed their suitability for CMOS/MEMS processes, and the first is even compatible with resin masking process.

The use of microwave tin oxide implemented by means of microprinting on silicon micromechanised integrated substrates allowed precise measurements and the verification of the implemented technologies. In this point, the use of **palladium catalysed active filter microwave SnO_2 allowed the quantification of CO and CH_4 in mixtures by means of a simplified algorithm**.

Moreover, we would like to mention other tasks that in spite of its leak of originality, becomes an advanced work in the field of semiconductor gas sensors:

- ✓ Design of two test stations for domestic and high temperature exhausts gas sensors.

- ✓ Implementation of grinding processes.
- ✓ Development of standard processes in printing, including active layer, passivation and circuitry.
- ✓ Design of substrate technology for alumina-based sensors.
- ✓ Design of heater in silicon micromachined silicon-based integrated sensors.
- ✓ Implementation of common muffle and furnace steps for common laboratory processes.
- ✓ Material Characterisation (XRD, XPS, FTIR, Raman, OA, AFM, SEM, XRF) of tin and titanium oxides pure and catalysed in powder and film sample.

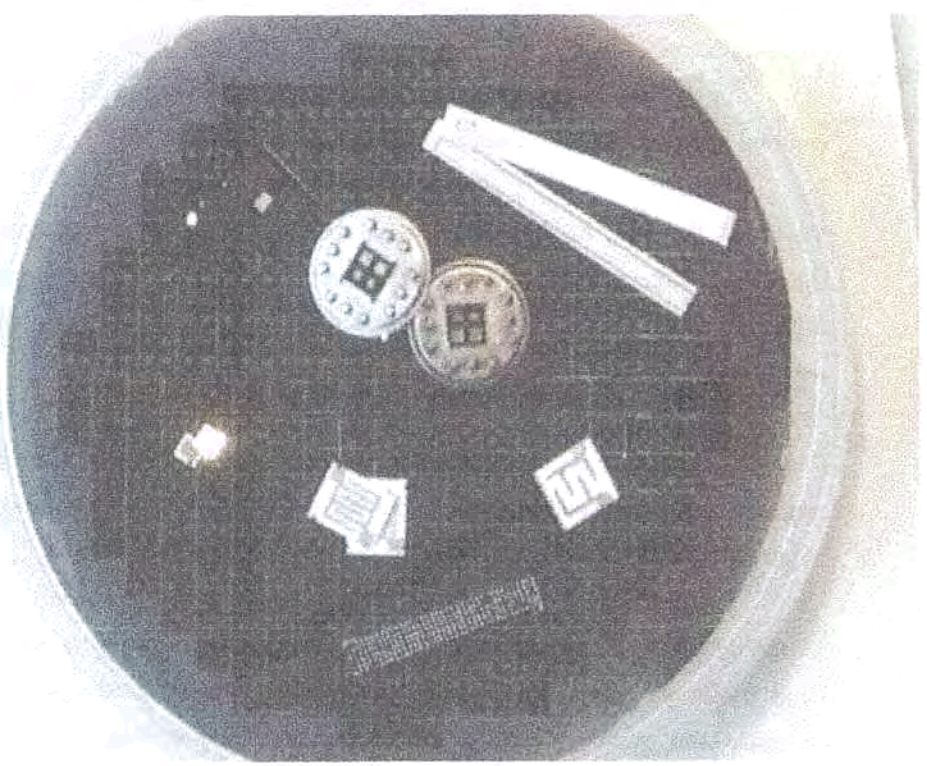

With all these new findings and developments, we consider that we have carried the tin oxide based sensors towards better positions in stability, selectivity, sensitivity and smart consumption ... however, there is still great leaks that should to be overcome. Let us review what of these leaks are present in this work.

The main self critic that scientist, specially those devoted to technological processes, can do is about the statistics of the processes ... in fact, when developing a new subject of research the goal is to arrive as far as possible, as soon as possible. And this is sometimes the origin of leaks of reproducibility.

To overcome these problems, besides the most careful sample preparation, in all this work, all the samples and sensors were made several times ... enough for scientific validation of the observed effects, not enough for their industrial implementation.

In this way, advanced studies of long-term stability are still needed to get an accurate understanding of the sensors performances.

Moreover, the study of the nanostructural evolution with the annealing temperature should be completed in the future with a correlation with the electrical properties of the different oxygen vacancy densities presented in the tin oxide samples, as well EPR measurements for the assessment of such densities.

Regarding the use of microprinting, this leads still to thick drops, which could be the origin of high electric consumption (about 100 mW). So, a reduction of this thickness is required.

The production of layers by means of pulverisation coating is one of the most promising ideas, but in our opinion its powerful application will be achieved when implemented tin oxide layer could be coated by a resin, and the silicon etching for micromachining could be done after. So, the challenge is launched.

Attending the production of the nanopowders, the most important question arises from the reliability of the chemical compounds for its development, some of them in assay production. Thus, variations in the water content of the *nominally* pentahydrated tin chloride could lead to changes in the catalytic content. Moreover, further work to standardise the production is still required.

With respect the study of the film samples, further experiments about the diffusion of gases through the sensing layer would be useful, as well as an improvement of the layer porosity. It would be also required a reduction of the catalytic density in the active layer in order to reach better sensing performances.

Finally, a better understanding of the catalytic effect in both CO and CH_4 by the tin oxide active catalytic filter need to be carried out in order to improve the sensors characteristics related with this effect.

Annex. Material characterisation

As a full description of the characterisation techniques and the apparatus can be found in [Diéguez,99], I will give only the experimental set-up and condition for material characterisation.

XRD (X-Ray Diffraction) patterns of powders were obtained with a Siemens D-500 x-ray diffratometer using Cu Kα radiation (λ=1.5418 Å), with operating voltage of 40 KV and current of 30 mA. Data were collected in steps of 0.025 degrees from 20 to 60 degrees (2θ) during 5 s of the measurement time per step. A secondary graphite monocromator was used in this instrument. In the case of sputtered films, XRD was performed with a Siemens D-500 instrument equipped with grazing incident attachment with a flat LiF monocrobmator. Similar experimental diffraction set-up parameters have been used for these samples. Spectra were analysed using the software Winfit [Krum,94] and considering Cu K_α radiation split for fitting.

XPS (X-ray Photoelectron Spectroscopy) data were collected with a physical electronics 5500 spectrometer under pressure $6x10^{-9}$ Torr. Al-K_α X-ray were produced with a physical electronics X-ray source, which produces photons with the energy of 1486.6 eV and natural line width of 0.9 eV. All the spectra were fitted to reach the right carbon position (284.5 eV) [Moulder,92][XPS,99]. The spectra were fitted with Gaussian-Lorentzian functions (80-20% respectively) and considering a Shirley baseline [Shirley,72]. Spectra were fitted with Multipak software [Multipak,98]

The Raman spectroscopy was performed in a Jobin-Ybon T64000 spectrometer coupled to an Olympus metallographic microscope. Excitation was provided by an argon-ion laser operation at a wavelength of 514.5 nm at an incident power of 2 mW.

Acquisition times were 12 minutes and the measurements ranged from 300 to 900 cm^{-1}. Raman shifts due to thermal effects were corrected by proper silicon reference (520 cm^{-1}) before each measurement.

AFM (Atomic Force Microscopy)

FTIR (Fourier Transform Infra-Red) transmission measurements were done with a BOMEM MB-120 spectrometer. The spectra were measured at room temperature, using normal incidence and a spectral resolution of 1.9 cm^{-1}. Absorption spectra from the samples were extracted by using the reference of air. The FTIR spectra from the powders were obtained by pressing them in KBr pellets. The FTIR CO/CO_2 consumption measurements have been performed by A. Cabot.

TEM (Transmission Electron Microscopy) –performed by J. Arbiol, Dr. A. Diéguez and Dr. A. Vilà-of the powders and thin film were carried out on a Philips CM30 SuperTwin electron microscope, operating at 300 KeV. For TEM observation, powders were ultrasonically dispersed in ethanol and deposited on amorphous carbon membranes. Cross-section electron transparent specimens of the thin SnO_2 layer were obtained by mechanical polishing and Ar^+ ion millinn at 5 KV, 0.6 mA and a beam incidence of 15°.

XRF (X-Ray Fluorescence) was performed with a Phillips model PW 1400, with an excitation source of Rh at 60KV. Two sequential crystals were used, LiF 220 and Germanium 111. A new Fischerscope instrument (system XDL) was tested in order to compare the reliability of the data.

References

In chronological order

[Shirley,72] D.A. Shirley, "High-resolution x-ray photoemission spectrum of the valence bands of gold", Phys. Rev. B, 5 (1972) 4709-4714.

[Moulder,92] J.F. Moulder, W. F. Stickle, P.E. Sobol, K.D. Bomben, "Handbook of x-ray photoelectron spectroscopy", Perkin-Elmer Corporation, Eden Prairie (1992).

[Krumm,94] S. Krumm, "A computer program for x-ray diffraction line profile analysis", Acta Universitatis Carolinae Geologica, 38 (1994) 253-261. Program available at www.geol.uni-erlangen.de/html/software/winsoft.html.

[Multipak,98] MultiPak V6.0A, Physical Electronics, Inc. (1998).

[Diéguez,99a] A. Diéguez, "Structural analysis for the improvement of SnO_2-based gas sensors", PhD thesis at the University of Barcelona (1999).

[XPS,99] XPS data tables, available at www.xpsdata.com

[SCT,00] Serveis Científico-Tècnics de la Universitat de Barcelona –*Scientific and Technique facilities at the University of Barcelona*-, information available at www.sct.ub.es.

Agraïments/Acknowledgements

Bé, ja tenia ganes d'arrivar aquí. Realment el camí ha estat llarg i turtuós ... o potser més que llarg, accelerat. Però no només pel descans i pau interior que presuposa escriure el punt final a un treball de quatre anys volia arribar a aquest apartat. En aquest temps he estat profundament afortunat en topar amb gent a la que he arribat a apreciar i estimar. Així doncs, tot i les ganes de deixar de banda l'ordinador, deixeu-me dedicar-vos unes paraules i, encara que segur que algú me n'oblido, sabeu que esteu tots en el meu record.

Deixeu-me en primer lloc, però, agrair a la Comissió Interdepartamental de Ciència i Tecnologia (CITIT) de la Generalitat de Catalunya el suport financer que mitjançant una beca FPI m'ha estat concedit. Igualment agraeixo a la Comisión Interministerial de Ciencia y Tecnología (CIRIT) el suport al projecte de recerca en el que he estat treballant.

Bé realment no sé per on començar ... bé sí, pel principi.

En primer lloc vull agrair al professor Dr. Joan Ramon Morante i Lleonart (Catedràtic del Departament d'Electrònica de la Universitat de Barcelona i director del mateix), no només el haver-me acollit al sí del Departament, sinó la seva estreta col·laboració durant aquests anys. Em treballat plegats en diversos temes de recerca i espero haver estat a l'alçada de les circumstàncies. T'he d'agrair especialment les interesants discussions que hem tingut sobre els fenòmens físics que hi havia en les mostres que hem estudiat.

Només espero que gaudisis de les discussions tant com jo.

En general a tots el membres del Departament d'Electrònica (Àlex, Olga, Paqui, Manolo, Blas, Manel, Arturo, Miguel Ángel, Òscar, Toni, Mauri, Sami, Albert, Sebas, Santi, Azzouz, Javier, Teo, Julio, Genís, Àngel, Manel, José María, Ángel, Gemma, Flavio, Sergio, Christophe, Rosa Maria, Frank, Beatriz, Jacobo, Oliver, Susanna, Àlex, Nourdin, Andrés, Paco, Joan, Enric, José Antonio, Manel, Pepe, ... l'Isidro que ens va deixar, els nou-vinguts i els que em deixi), ja que sou un grup de gent molt maca, com ho demostra la magnífica convivència al Departament, tot i ser un grup nombrós.

Més concretament vull manifestar la meva convicció de que treballo en un grup excepcional, dedicat a sensors de gas. En Jaume Folch, l'Ana Ruíz, l'Andreu Cabot, en Raul Díaz, en Jordi Puigcorbé, en Jordi Arbiol, l'Ismael Jiménez, la Judith Cerdà i la Dra. Anna Vilà...a tots vosaltres us he de dir que sense la vostra col·laboració, no hauria pogut engegar aquest projecte. Encara més, és un plaer treballar al costat vostre cada dia ja que em doneu la possibilitat d'aprendre amb vosaltres, tot i mantenint una relació humana que estic segur que qualsevol envejaria per sí mateix.

Als companys de FAE –Sr. Manuel Rodrigo, Sr. Francisco Marro, Sr. Gabriel Renom, Sr. Francisco Ramos-, també els hi vull agraïr la seva amistat i la confiança que han depositat en nosaltres. L'estreta col·laboració que hem tingut aquests anys ha servit per a forjar quelcom més que una interesant relació Universitat/Empresa, sinó un nexe comú entre persones que volen aprendre i desenvolupar.

I would like to thank Dr. Nicolae Bârsan and Dr. Udo Weimar from the University of Tübingen for a close relationship and enlightening discussions during my research stage in their University.

También quiero agradecer a mis compañeros del Centro de Estudios e Investigaciones Técnicas de Guipuzcoa –Prof. Dr. Javier Gracia, Prof. Dr. Enrique Castaño y Gemma García- su colaboración en el trabajo conjunto que hemos desarroyado en el presente proyecto de investigación. A Yago Olaizola (sí, *doctor*, que no me olvido) le quiero dedicar un agradecimiento sincero, ya no sólo por su colaboración científica y su gran valor como tecnólogo, sino por la estrecha amistad y cordialidad que me ha brindado en todo momento.

Però, si hi ha algú que realment m'hagi impresionat durant aquests anys ha estat el meu director de tesi, Prof. Dr. Albert Cornet Calveras ... Albert, deixa'm agrair-te de forma molt especial tot el que has fet per mi. En aquests quatre anys has tingut cura i preocupació de tot el que passava. Has tingut oida per a escoltar-me i paciència per a pensar-hi. M'has recolçat quantes vegades he necessitat i m'has sabut orientar de manera que m'he sentit realment bé i agust realitzant la meva tasca. I, ara, en aquests mesos, m'has ajudat extraordinàriament en la realització d'aquesta memòria de tesi. Però lo que més em sorprén, i per lo que més t'elogio, és per qué sé que tot això ho fas per a tothom a qui pots ajudar... Albert, si ets un científic i professor de gran vàlua i reconegut prestigi, et puc dir que la teva característica humana és absolutament insuperable.

Bé, ja veieu que he sigut molt afortunat ... però, la principal font de felicitat me l'ha donat tres persones, els meus pares i la meva dona.

Joan i Pilar ... pares, us vull agraïr tot el que heu fet per mi i de la forma en que m'heu educat. Em sento una persona honesta i autosuficient, i sé que vosaltres sou els responsables d'això. També sé que desitjaveu de tot cor que el vostre fill tingués una educació, la qual la mala fortuna va negar a la vostra generació. Heu lluitat fortament per alguna cosa, i en la mesura de lo que us pugui recompensar, espero que aquesta tesi us ajudi a sentir-vos una miqueta millor.

Sonia, a ti quiero dedicarte mi más profunda felicidad que he compartido contigo durante estos años. Has sido un continuo aliento y una bocanada de aire fresco cada mañana ... y un suspiro de alivio al verte cada atardecer. No sé si hubiese hecho este trabajo sin ti, pero de lo que sí que estoy seguro es de que no sería tan feliz.

Déjame agradecerte, también, tu ayuda durante estos meses, que sé que han sido difíciles. Estar al lado de alguien que sólo piensa en su tesis es extraordinariamente complicado, mas cuando la urgencia y el exceso de trabajo acosan. Saber lo que se debe hacer en cada momento es complejo, nunca hay forma humana de saberlo. Sólo espero poder ayudarte tanto como lo has hecho tu.

Resum

1. Introducció

En la nostra societat, l'anomenada Societat de la Informació, els sensors tenen una importància cabdal. Dintre d'aquests, el sensors de gasos estan relativament poc desenvolupats degut a la dificultat intrínseca del fet de distingir diferents gasos.

En l'actualitat diferents tipus de sensors són comercialment disponibles, d'aquests només el sensors d'estat sòlid mantenen una relació qualitat/cost que els fa interesant per a aplicacions massives.

1.1 Panoràmica

Dintre dels sensors d'estat sòlid –índexats a la taula 1-, els més desenvolupats són el Sensors Semiconductors de Gas, que són aquells en que la presència d'un gas indueix un canvi de resistència.

Sensors capcitius i de conductància	
Resistències R	$R= f(p_i)$
Capacitats C	$C=f(p_i)$
Conductància depenent de la freqüència Y	$\|Y\|=\|G+i\omega C\|=f(p_i)$
Sensors d'efecte camp	
Potencials ΔV	$\Delta V=f(p_i)$
Corrent font-drenador I_D	$I_D=f(p_i)$
Canvi en funció de treball $\Delta\phi$	$\Delta\phi=f(p_i)$
Sensors calorimètrics	
Calor de reacció Q_{react} per temps	$\Delta V \sim Q_{react} \sim \Delta P \sim r\Delta H = f(p_i)$
Sensors optoquímics	
Constants òptiques ε	$\varepsilon(\nu)=f(p_i)$
Funció de freqüència ν	
Intensitat de llum I	
Sensors sensitius de massa	
Masses Δm de partícules ad- or absorbed	$\Delta f=-C_f f_0^2/A\cdot\Delta m=f(p_i)$

Sensors d'electròlit d'estat sòlid	
Voltatges V	$V=(RT/nF)\ln a_i$
Corrents I	$I=(nFAD a_i)/\delta$

Taula 1. Visió genèrica dels sensors de gas d'estat sòlid.

Al seu torn, l'impacte econòmic i de desenvolupament industrial d'aquest tipus de sensors és elevat considerant que són el que generen un major número de vendes per any.

1.2 Sensors Semiconductors de Gas

El sensors semiconductors de gas semiconductors es basen en les propietats d'alguns òxids metàlics, com l'òxid d'estany o titani, capaços de variar la seva resistencia en ser exposats a un gas. Així, la seva resposta es mesura com

$$S = \frac{R_{air}}{R_{air} - R_{gas}}$$

funció que dóna compte de les variacions de la resposta del sensors (S) envers el gas.

Per a obtenir una resposta satisfactòrica, cal escalfar el material sensor fins a aconseguir temperatures de l'ordre de 400°C, amb la qual cosa les derives estructurals del material sensor exposat a atmosferes amb diverses composicions gasoses esdevenen molt crítiques.

Dones aquestes condicions de treball, la problemàtica d'aquest tipus de sensors es basa en el que s'anomena les *4 s*:

- ✓ Estabilitat. Cal que la resposta del sensor sigui estable a mig i llarg termini d'operació per tal de donar garanties d'exit en funcionament.

- ✓ Sensibilitat. Les respostes de canvi de resistència (S) han de ser suficientment grans com per a poder quantificar les concentracions de gasos presents en l'atmofera a controlar.
- ✓ Selectivitat. Cal que el sensor no dongui falses alarmes com a conseqüència de gasos interferents. Així, cal que el sensor distingeixi selectivament els gasos a mesurar.
- ✓ Consum inteligent. A tot això cal afegir-hi que el consum elèctric ha de ser minimitzat per a rebaixar costos, tant productius com de manteniment.

1.3 Esboç de la tesi

En aquest context, l'objectiu de la tesi és la millora de les caracterítiques sensitives dels dispositius sensors semiconductors de gas basats en òxid d'estany nanocristal·lí.

Per a aquesta millora, es desenvoluparan noves tecnologies (piròlisi líquida i tractament per microones) per a l'obtenció de l'esmentat material sensor. Aquest òxid d'estany serà implementat mitjançant noves tècnques (microimpresió i recobriment per pulverització) en substractes micromecanitzats de silici.

En el seu conjunt, la tesi consta de sis capítols, incloent-hi les conclusions:

- ✓ En el primer capítol es presenta la panoràmica del sensors de gas en el context social i tecnològic actual. També s'aporta una breu descripció de la tesi.
- ✓ El segon capítol està dedicat a donar una visió genèrica tant dels aspectes tecnològics com a de funcionament dels sensors semiconductors de gas basats en SnO_2

- ✓ En el tercer capítol es presentent les noves tecnologies desenvolupades per a l'implementació del material sensors en substractes micromecanitzats, així com el sistema de test per a la verificació del correcte funcionament d'aquests sensors.
- ✓ El quart capítol està dedicat a la presentació de les principals característiques de la pols d'òxid d'estany obtinguda mitjançant piròlisi líquida o tractament de microones.
- ✓ En el cinquè capítol s'aplica tot el coneixement de caracterització de materials desenvolupat en el quart capítol per a l'estudi les capes primes d'òxid d'estany.
- ✓ Finalment es presenten les conclusions de la tesi.

2. Sensors de gas semiconductors basats en SnO_2 nanocristal·lí, una visió global.

2.1 Aspectes generals

Els sensors semiconductors de gas consten de una capa sensora, que pot estar composta de diferents òxids metàl·lics com el SnO_2, d'elèctrodes, d'un sistema d'escalfament i d'un element de subjecció anomenat substrat.

En l'actualitat s'utilitzen diferents tècniques per a l'obtenció i/o implementació d'aquest òxid d'estany en l'element sensor –veure taula 2-.

Producció de material sensor	Implementació sobre sensors
Sol-Gel	Sinterització
Processat de microones	Impressió
Piròlisi líquida	Recubriment per rotació
Mètode hidrotèrmic	Recubriment per pulverització
Piròlisi làser	Immersió
Ablació làser	
Producció i dipòsit de material sensor	
Tècniques químiques	Tècniques físiques
Spray piròlisi	RGTO
Piròlisi líquida	PVD

Taula 2. Tecnologies per a la producció, dipòsit i implementació de SnO_2.

Al contrari del que es podria pensar, la utilització d'una o altra tècnica en combinació amb diferents tipus i/o configuració de sensors dóna lloc a unes característiques sensors

molt diferents. Aquesta problemàtica, que podríem anomenar de disseny, s'afegeix a les anteriors problemàtiques mostrades pels sensors semiconductors de gas. Per això es fa necesari un coneixement profund de la situació actual del sensors de gas basats en SnO_2, com es mostra a aquest capítol.

2.2 Materials sensors

S'ha demostrat que el canvi de resistivitat dels òxids metàlics en ser sotmesos a diferents atmosferes es una característica comuna a la major part d'aquests.

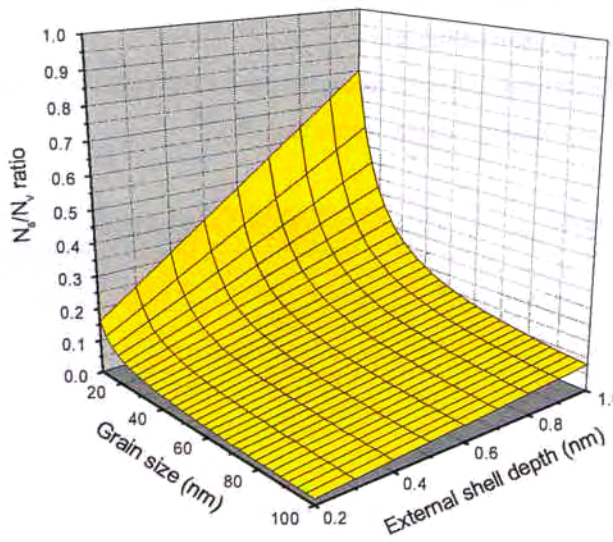

Figura 1. Contorn del gra repecte a l'interior de gra respecte a la mida de gra .

Entre aquest òxids existeix una característica comuna d'avidesa per l'òxigen atmosfèric capaç de compensar les vacants d'oxigen que de forma naturual hi ha en l'òxid. Quan altres gasos entren en competència i/o reacció amb l'òxigen, el material reacciona exhibint un canvi de resistivitat.

Desde un punt de les caracterítiques microestructurals del material sensors, s'ha demostrat que la utilització de nanopartícules incrementa la sensitivitat del material sensor envers els gasos. De

forma simple, es pot demostrar que la quantitat de superfície específica augmenta quan disminueix la mida de gra. Així podem avaluar la quantitat d'àtoms a la superfície del gra (N_S) sobre el número d'àtoms residents a l'interior (N_V) com

$$\frac{N_S}{N_V} = \frac{4(D/2)^2}{r^2}\,\frac{r^3}{\left(\frac{1}{2}D\right)^3} = \frac{8r}{D} = \frac{0.8}{D}\,nm$$

on D és la mida de gra i r la profunditat de l'escorça exterior . A la figura 1 podem veure com augmenta la relació d'àtoms a la superfície quan disminuexi la mida de gra.

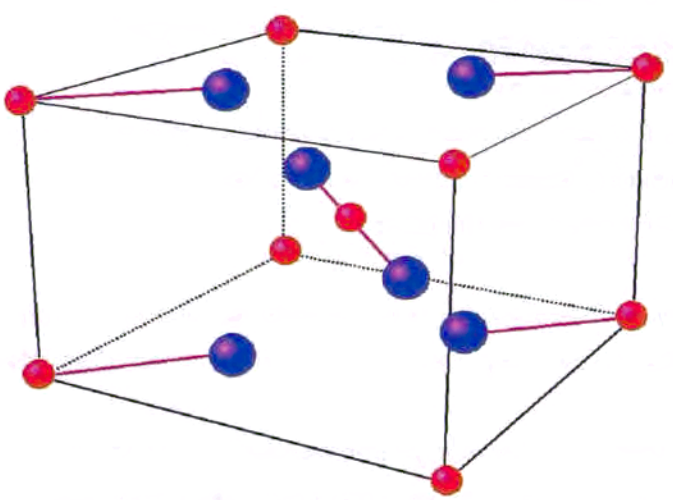

Figura 2. Estructura Rutil del SnO_2. Els atoms més grans representen l'oxigen.

Dintre dels òxids semiconductors, l'òxid d'estany és el més utilitzat tant a nivell científic com comercial.

Un anàlisi produnt de les seves caracterísques revela una alta estabilitat de les propietat elèctricques derivades del seu alt grau d'ionicitat.

A la figura 2 es pot apreciar l'estructura de la cel·la unitat de l'òxid d'estany. La corresponent estructrua cristal·lina és rutil.

2.3 Configuracions i dissenys de sensors

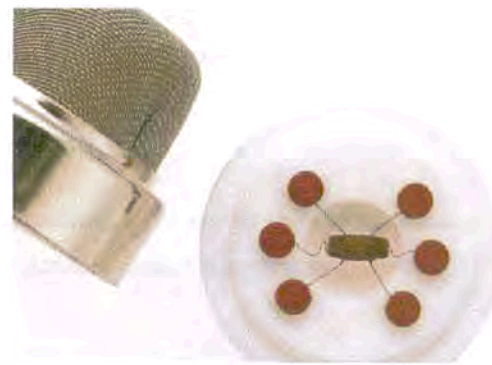

Figura 3. Sensor tipus Taguchi

El desenvolupament del sensors de gas semiconductors ha començat des del punt de vista comercial en els anys 60. En aquesta època es va ençetar la producció del sensors tipus Taguchi –figura 3-.

Els sensors tipus Taguchi es composen d'un cilindre amb interior buit a on hi està allotjat una resistència calefactora. A l'exterior s'hi sinteritza l'òxid d'estany semiconductor. Les principals problemàtiques d'aquests sensors consisteixen en la complexa industrialització del procés de fabricació del sensor i en l'ineficaç escalfament del material sensor.

Una millora del diseny ha consistit en la planarització del substracte ceràmic, on tant calefactor com elèctrode estan impressos, tècnica per la qual també s'hi implementa el material sensor.

Però una revolució molt més important s'ha aconseguit mitjançant la utilització de sensors micromecanitzats. Aquests sensors permeten a altes temperatures zones molt localitzades amb baixes perdues d'escalfor, de tal manera que es possible arribar fins a 300°C amb aproximadament 40 miliwats.

2.4 Descripció genèrica dels models de sensitivitat

The forma genèrica, la resposta del sensors de gas pren formes del tipus,

$$\frac{R_{o,d}}{R_{g,d}} = 1 + A_g \left(\frac{P_{gas}}{P_{aire}} \right)^{1/n}$$

on $R_{o,d}$ és la resistència en aire sec (P_{aire}) del sensor considerat, i $R_{g,d}$ la resitència en gas del sensors P_{gas}. A_g denota la sensitivitat en aire sec. L'exponent *n* depén del gas, del material sensor i de la catalització. Així, per a SnO_2 pur captant CO o CH_4 , el coeficient pren un valor de 2.

Aquest tipus de resposta pot ser modelitzada mitjançant un esquea de reacció del tipus

$$\tfrac{1}{2}O_2 \leftrightarrow O_s \leftrightarrow O_2^- \leftrightarrow \begin{array}{l} 2OH^- \\ \updownarrow H_2O + e^- \\ O^- \\ \downarrow \\ RO \end{array} \leftrightarrow O^{2-}$$

on la molècula d'oxigen es disociada a la supeficie del material sensor en ser fisisorbida. Posteriors transvassaments de càrrega del material sensors a la molècula permeten una quimisorpció que finalment pot donar lloc a reaccions amb altres molècules de gas i, fins i tot grups hidròxils. Aquestes darreres reaccions són les que donen lloc als canvis de resistivitat del material sensor.

Igualment es possible definir una cinètica per a aquestes reaccions, com per exemple

$$\frac{m}{2}O_2^{(g)} + Ie^- + S \underset{k_{-1}}{\overset{k_1}{\rightleftarrows}} O_{ms}^{I-}$$

$$mCO^{(g)} + O_{ms}^{I-} \xrightarrow{k_2} mCO_2^{(g)} + Ie^- + S$$

aquesta cinètica dóna lloc a una quantificació de la quantitat d'oxigen recobrint la superfície del material sensor (θ), de la que la resistivitat n'es funció,

$$\theta = \frac{\dfrac{2n_s^2 k_1 k_2 [O_2]}{k_4 [CO]} + k_1 n_s [O_2]}{k_{-1} + k_2 n_s}$$

Una descripció més detallada d'aquesta resistivitat s'assoleix mitjançant la introducció de la barrera de potencial que apareix a l'espai intergranular,

$$V_s = \frac{-eN_s^2}{2\varepsilon\varepsilon_0 N_D}\left[1 + \exp\left(\frac{E_s - E_F}{KT}\right)\right]^{-2}$$

Amb aquesta barrera de gra és possible calcular la densitat de corrent termoiònic entre grans com

$$J_T = -en_b\left(\frac{KT}{2m^*\pi}\right)^{1/2}\exp\left(\frac{eV_s}{KT}\right)\left[\exp\left(\frac{-eV_a}{KT}\right) - 1\right]$$

on V_a és la tensió entre nanograns. Si considerem un número G de nanocristall molt elevat tenim

$$\frac{eV_a}{G} << KT$$

i podem aproximar,

$$J_T \approx e^2 n_b\left(\frac{1}{2m^*\pi KT}\right)^{1/2}\exp\left(\frac{eV_s}{KT}\right)V_a$$

d'on podem derivar la conductivitat com

$$\sigma = e^2 n_b \left(\frac{1}{2m^* \pi KT} \right)^{1/2} \exp\left(\frac{eV_s}{KT} \right)$$

I substituint a l'expresió de la barrera Schottky, obtenim una expressió simple per a la conductivitat en funció del recobriment d'oxigen:

$$\sigma = e^2 n_b \left(\frac{1}{2m^* \pi KT} \right)^{1/2} \exp\left\{ \frac{-e^2 I S^2 \theta^2}{8\varepsilon\varepsilon_0 n_b KT} \right\}$$

3. Tecnologia i sistemes de test en sensors de gas semiconductors.

3.1 Procediment estàndard pel processat de pols

Tot i no haver-hi una metodologia estàndard pel processat de pols d'òxid d'estany, està comunment acceptat que diferents tractaments han de ser aplicats sobre el material sensor per a augmentar la sensitivitat, selectivitat i estabilitat.

Una vegada s'obté el material sensors, aquest pot exhibir importants derives de tipus estructural sota les altes temperatures d'operació. En conseqüència, es requereix d'una estabilització tèrmica per a evitar aquesta problemàtica.

Però aquesta estabilització tèrmica o recuit dóna lloc a un material aglomerat que exhibeix colls entre grans. El consegüent pobre grau de porositat del material influeix negativament en la difusió de gas en el material sensor i per tant en la resposta del dispositiu sensor. Per aquest motiu, s'ha de dur a terme un procés de molturació després del tractament tèrmic.

Finalment la implementació de la pols sobre substractes ceràmics per a obtenir el dispositiu sensors pot ser desenvolupada mitjançant una tècnica estàndar d'impresió la qual dóna resultats molt reproductibles.

Tots aquests processos han estat implementats en el nostre laboratori.

3.2 Tecnologia pel dipòsit mitjançant sputter

El dipòsit d'òxid d'estany en capa prima (film) mitjançant sputter (pulverització catòdica) ha sigut realitzat sobre oblies de silici am elèctrodes interdigitats i escalfador.

El procés consisteix en l'oxidació de l'oblia. A continuació es diposita el crom i el platí que constitueixen l'escalfador, que es perfila mitjançant fotolitografia. Per aillar el material, s'hi deposita sobre el platí una capa aïllant de SiO_2. Finalment els elèctrodes -compostos també de Cr/Pt- hi són dipositats. A la figura 4 s'hi pot observar l'aspecte del microsensor i un esquema del mateix.

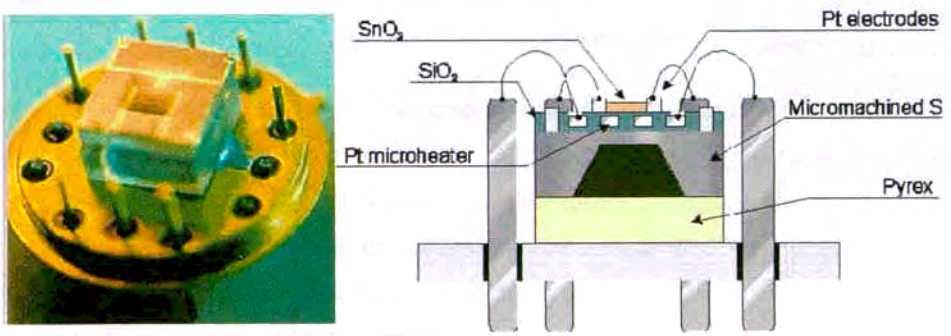

Figura 4. Esquerre, sensors desenvolupats. Dreta, esquema del microsensor.

3.3 Tecnologia de substrats per a la implementació de pols

En paral·lel al disseny de sensors micromecanitzats en tecnologia de silici per a dipòsit mitjançant pulverització catòdica, s'han dissanyat substractes en base ceràmica (alúmina) i silici per a la implementació mitjançant impressió, microimpressió i

recubriment per pulverització de les pols d'òxid d'estany obtingudes per microones i piròlisi líquida.

Dintre dels sensors en base ceràmica, tres dissenys han estat duts a terme.

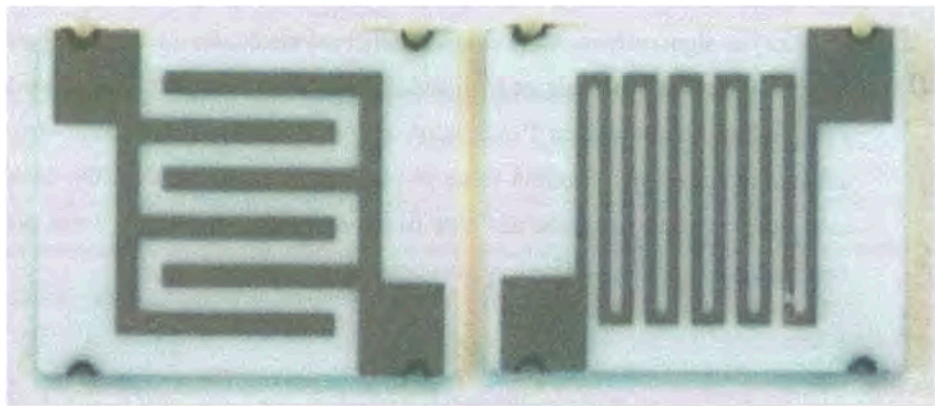

Figura 6. Disseny de substracte en base ceràmica.

Aquests sensors consten de dues cares a les quals hi el escalfador i l'elèctrode per a mesura elèctrica. No obstant, les dimensions d'aquests (aprox. 10x10 mm^2) i el seu gruix (0.6 mm) fan que les disipacions de potència siguin extraordinàries i que calgui un consum molt elevat per a aconseguir temperatures moderades.

Per aquest motiu es procedeix al disseny d'un microsensor amb colaboració amb el Centro Nacional de Microelectrónica (CNM a Bellaterra). El disseny obtingut millora altament el rendiment energètic i permet escalfar a 400°C amb un consum inferior a la dècima de watt.

3.4 Noves tècniques d'implementació de nano-pols prèviament estabilitzada

Un cop es disposa de la pols d'òxid d'estany i dels substractes a on ha de ser dipositada, cal implementar-la. En ser les tècniques d'implementació disponibles comercialment – impressió i immersió- no adequades per al nostre propòsit, es procedeix al desenvolupament de dues noves tècniques: microimpressió i recobriment per pulverització. A la taula 3 hi presentem un estudi comparatiu de les dues tecnologies.

	Microimpressió	**Recobriment per Pulverització**
Tecnologia basada en	Impressió	Spray
Control sobre	Volum dipositat	Gruix dipositat
Manca de crontrol	Gruix dipositat	Superfície dipositada
Necessitat de màscares	No	Sí
Pas d'implementació	Substracte encapsulat	Despres de màscara
# sensors per procés	1	Whole wafer
Posterior estabilitzció per	Autoescalfament	Autoescalfament o forn
Compatibilitat amb resines	Mitjà	Alta
Compatibilitat amb màscares físiques	Nul·la	Molt Alta
Repetibilitat	Alta	Molt Alta
Dificultat de control	Mitjana	Alta
Aplicabilitat sobre substracte de silici	Sí	Sí
Aplicabilitat sobre alúmina	No	Sí
Automatització actual	Baixa	Alta

Taula 3. Comparació tecnològica entre microimpresió i recobriment per pulverització..

Mentre el recobriment per pulverització es basa en l'atomització d'una disolució que conté el material sensor que en arribar al substracte prèviament escalfat s'hi queda adherit, la microimpresió es basa en la transferència d'un fluid que conté el material sensor des d'un capilar fins a la membrana micromecanitzada del microsensor.

3.5 Sistema de test per a dispositius sensors

Un cop implementat el material sensor, el dispositiu està llest per a mesurar. Per a aquest propòsit s'han desenvolupat 3 sistemes de test.

En primer lloc s'ha dissenyat un sistema portàtil capaç de generar atmosferes en base d'aire sintètic –sec o humit- amb concentracions de CO fins a 1000 ppm i de NO_2 fins a 10 ppm. Aquest sistema bàsicament està orientat a la realització de caracterització in-situ i de mesures elèctriques simples.

En segon lloc es dissenya una estació automatitzada per a sensors de gas d'alta temperatura, com poden ser els sensors de gasos exhausts. Aquest sistema es basa en la generació d'una barreja de gasos –mitjançant controladors de flux màssic-. Aquesta barreja, parametritzada mitjançant el paràmetre λ que dóna idea de la riquesa de mescla en una combustió es pot reduir a una expressió com

$$\lambda = \frac{[CO_2]+[CO]/2+[O_2]+\left\{\frac{3.5}{3.5+[CO]/[CO_2]}\right\}([CO_2]+[CO]+[NO]/2)}{2([CO_2]+[CO]+[CH_4])}$$

d'on es pot extreure que amb una certa concentració de CO_2, CO, O_2, NO i CH_4 podem simular una atmosfera exhausta.

Finalment es dissenya i construeix una estació de test per a sensors medioambientals. Aquesta estació cobreix les necessitats de la primera estació, però amb tots els aventatges d'automatització i adquisició de dades de la segona estació. D'aquesta manera, es factible controlar la humitat de la barreja (fins el 80%), la concentració de CO (fins a 1000 ppm), de CH_4 (fins a 10000 ppm) i de NO_2 (fins a 10 ppm).

4. Sensors basats en òxid d'estany nanocristal·lí en forma de pols

4.1 Introducció

En aquesta secció es presenten les noves tecnologies per a l'obtenció de nanopartícules d'òxid d'estany així com la seva caracterització atenent la temperatura de recuit com principal font de variacions en la nanostructura del material. Finalment es verifica la fiabilitat dels sensors implementats i s'obté un algoritme de càlcul de concentració de CO i CH_4 en barreges binàries.

4.2 Dues noves tècniques per a la producció d'òxid d'estany nanostructurat

Atenent a les consideracions sobre la mida de gra de l'òxid d'estany que es pot desenvolupar per tècnologies clàssiques (sol-gel, mètode hidrotèrmic) es desenvolupen dues noves tecnologies que produeixen pols de SnO_2 amb unes característiques idònees per a la producció de sensors de gas.

Les tècniques d'obtenció de material sensor bàsicament són adaptacions de tecnologies que en el camp de l'electrònica o la química s'utilitzaven amb anterioritat. Així és possible obtenir una capa de material sensor amb pulverització catòdica (*sputtering*) o pols del material sensor mitjançant procés químic de *sol-gel*.

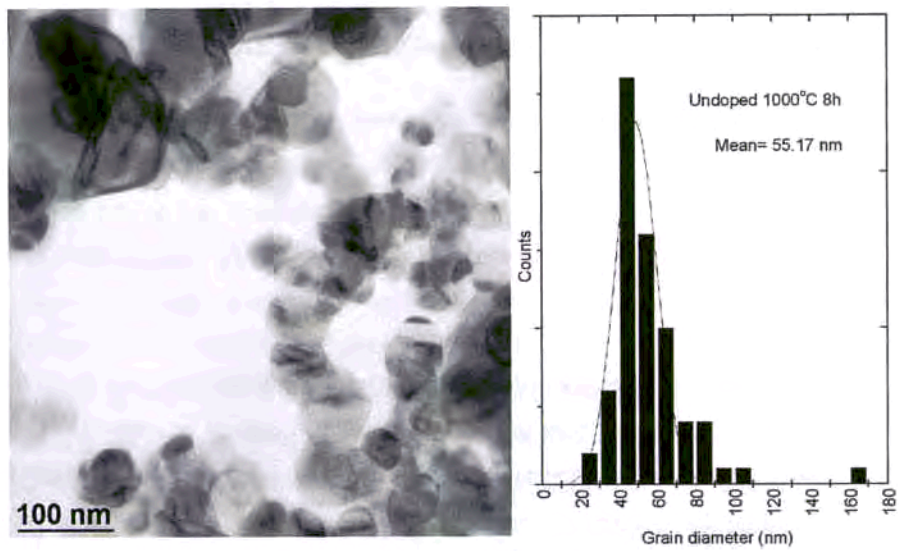

Figura 7. Esquerra, fotografia mitjançant microscòpia electrònica de transmissió de les nanopartícules d'òxid d'estany obtingutdes mitjançant tractament de microones. Dreta,

En treballar el material sensor a altes temperatures, és recomanable estabilitzar-lo tèrmicament abans d'utilitzar-se. Així són necessaris tractaments de 400 a 1000°C durant hores. Però aquests tractaments es veuen molt limitats en el cas d'obtenció d'una capa. Igualment, les tecnologies químiques inverteixen gran quantitat de temps per a l'obtenció de petites quantitats de pols de material sensor. Dues noves estratègies, basades en una reacció química similar, s'han desenvolupat per a solventar aquestes problemàtiques. En primer lloc s'ha obtingut òxid d'estany nanomètric per descomposició i reoxidació de $SnCl_4$ mitjançant radiació de microones. Aquesta nova tecnologia permet obtenir material sensor d'unes característiques idònies per a la sensitivitat. Així, la mida de gra és d'uns 55 nanòmetres –veure figura 7- en aplicar-hi tractaments tèrmics de 1000°C durant 8 hores. Aquestes dades són aproximadament la meitat que les reportades en la literatura per a processos com el sol-gel.

Un procediment alternatiu a aquest consisteix en la combustió controlada del clorur d'estany mitjançant escalfament convencional. En aquest sentit, una millora substancial de les característiques del material sensor s'obté quan aquest escalfament és

induït en petites quantitats aïllades de clorur que faciliten la reoxidació posterior, procés batejat com piròlisi líquida.

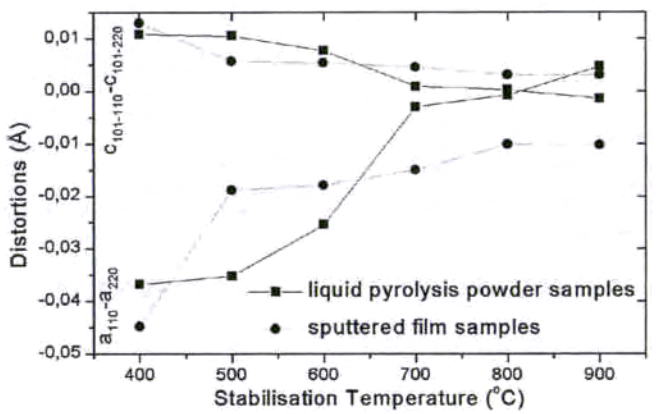

Figura 8. Còmput de la distorsió cristal·lina per a SnO_2 en pols i en capa.

Una anàlisi detallada de les propietats microestructurals d'aquest material sensor en funció de la temperatura d'estabilització ha permès establir que a partir de temperatures 700°C esdevé completament estable i amb una cristal·linitat suficientment bona com per a considerar que el material no patirà –en aquest aspecte- derives temporals que puguin repercutir en el vessant sensor. Com s'aprecia en l'anàlisi de distorsions de xarxa de la figura 8, aquesta característica que es dóna en les mostres de piròlisi líquida no es presenta en altres obtingudes per *sputtering*.

Aquestes notables característiques microstructurals del material obtingut redunden en unes adequades propietats elèctriques, com es pot apreciar a la figura 9, on s'hi ha representat la resposta de sensors d'òxid d'estany obtingut mitjançant piròlisi líquida i catalitzats amb pal·ladi.

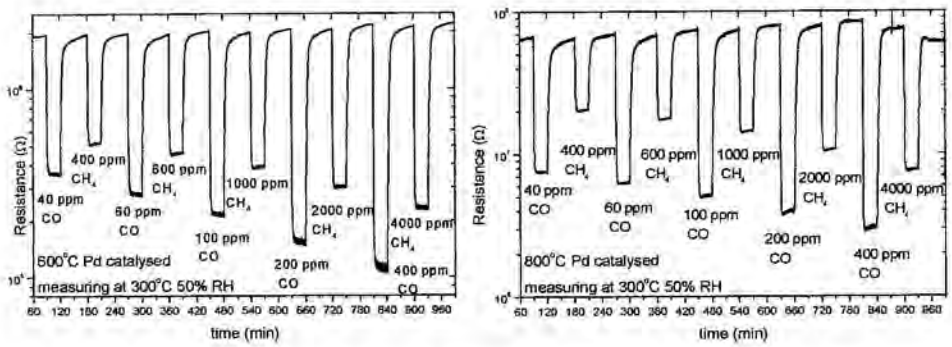

Figura 9. Resposta del sensor a polsos de CO i CH_4. Esquerra sensors recuit a 600°C. Dreta, 800°C.

4.3 Evolució nanostructural del SnO_2 amb la temperatura de recuit

Sembla acceptat que les característiques estructurals i elèctriques del SnO_2 han d'influenciar fortament la sensitivitat. Al seu torn, la nanoestructuració ha esdevingut experimentalment un punt important en el desenvolupament dels sensors de gas semiconductors.

Diversos estudis han aprofundit en l'estructura electrònica associada als defectes d'oxigen en l'òxid d'estany. Altres estudis, recents i innovadors, han estudiat la nanoestructura d'òxids metàl·lics des del punt de vista de la difracció de raigs X i l'espectroscòpia Raman, associant noves característiques estructurals a la nova dimensionalitat de la matèria.

En el present apartat es pretén relacionar experimentalment els efectes de la incorporació d'àtoms d'oxigen a la xarxa cristal·lina de SnO_2 amb la nanoestructura observada a les mostres 5M (principalment) obtingudes per piròlisi líquida.

Es possible observar un important canvi en el grau de cristal·linitat en les dades de XRD. Es possible observar també aquest efecte en les dades d'espectroscòpia Raman.

Com pot apreciar-se a la figura 10, la intensitat de les reflexions (220) i (110) creix respecte a (101) i (211). Aquesta variació suggereix un important canvi en la morfologia dels corresponents plans atòmics. Amb referència a l'estructura rutil (figura 2), mentre els plànols (101) i (211) contenen un promig alt d'àtoms de Sn, els plànols (110) i (220) estan formats per una proporció més alta d'àtoms d'oxigen.

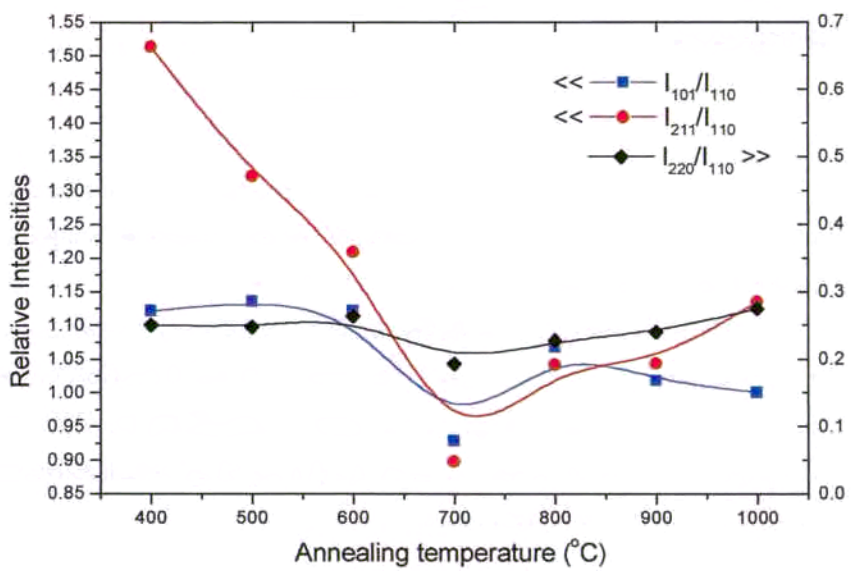

Figura 10. Intensitats relatives dels difractogrames de les mostres 5M obtingudes a diferents temperatures.

Aquest raonament, que està indicant que els efectes de la incorporació d'oxigen són més presents en aquells plans que relativament en contenen més densitat. En aquest cas el mètode experimental era tal (spray piròlisi) que es procedia a una incorporació de Sn.

Això induïa a pensar que amb la temperatura es produïa una relaxació d'àtoms d'estany intersticials cap a posicions de la xarxa. Aquesta relaxació es traduïa en un decreixement de la reflexió (200). En el nostres cas partim d'una situació en la qual tenim la totalitat d'àtoms de Sn i haurem de completar l'estequeometria del compost incorporant àtoms d'oxigen. Això portarà a relaxar, doncs, les vacants d'oxigen.

Per tal de simular els efectes de les vacants d'oxigen, procedirem a un anàlisi dels factors d'estructura del material. Podem escriure aquests darrers com

$$F_{hkl} = \sum_{j}^{cel\cdot la\ unitat} f \exp\{2\pi i(hx_j + ky_j + lz_j)\}$$

on x_j, y_j i z_j es la posició de l'àtom j-èssim a la cel·la unitat i f_j és el factor de scattering determinat per,

$$f = f_{corr} \exp\left\{-\frac{B_j \sin\theta}{\lambda^2}\right\}$$

El terme exponencial correspon a la correcció pel factor de temperatura de Debye-Waller. f_{corr} representa el factor de scattering (sense correcció de temperatura) amb la correcció per a dispersions anòmales.

Per a simular els efectes de les vacants, considerarem l'existència de (1-α) ratio de vacants sobre posicions d'oxigen en una cel·la unitat, uniformement repartides. És a dir, α representa el factor d'ocupació dels àtoms d'oxigen a les seves posicions. Això fa que puguem escriure els factors de scattering promig de les posicions corresponents als oxígens en primera aproximació com,

$$f_O^T \approx \alpha f_O + (1-\alpha) f_{vac}$$

Per simplicitat, i considerant una densitat de càrrega nul·la al voltant de la vacant d'oxigen, prendrem $f_{vac} \approx 0$. Aquestes dues aproximacions seran més vàlides

conforme $\alpha \rightarrow 1$. D'aquesta manera, i atenent a les posicions atòmiques de l'òxid d'estany obtenim que,

$$F_{hkl} = 2f_{Sn} + 4f_O \alpha \cos(2\pi hx)\cos(2\pi kx)$$

$$\text{si} \qquad h+k+l = \text{imparell}$$

$$F_{hkl} = -4f_O \alpha \sin(2\pi hx)\sin(2\pi kx)$$

$$\text{si} \qquad h+k+l = \text{parell}$$

on la constant estructural x val 0.304. Per a les reflexions analitzades obtenim uns factors d'estructura,

$$F_{110} = 2f_{Sn} + 0.443 f_O \alpha$$
$$F_{220} = 2f_{Sn} + 2.424 f_O \alpha$$
$$F_{211} = 2f_{Sn} + 1.036 f_O \alpha$$
$$F_{101} = 2f_{Sn} - 1.331 f_O \alpha$$

Numèricament es pot apreciar com la constant que acompanya el factor de scattering de l'oxigen és especialment alta en el cas de la reflexió (220). Per a explicar la diferència numèrica entre les reflexions (220) i (110) hem d'esmentar el treball de Matsuhata *et al* [Matsuhata,94]. Aquest autors, mitjançant mesures de difracció d'electrons d'alta energia, confirmen experimentalment que la reflexió (110) depèn molt més del grau d'ionicitat del Sn, mentre que la reflexió (220) rep una àmplia contribució de l'oxigen.

D'aquesta manera, triem la intensitat relativa I_{211}/I_{220} perquè, degut a la proximitat de les reflexions i en voler analitzar els efectes relatius en la reflexió (220), ens permet menysprear els efectes del factor de temperatura. Procedint amb les dades trobades a les taules de XRD per els factors de scattering podem aproximar,

$$\frac{I_{211}}{I_{220}} \approx \frac{|71.36 + 4.48\alpha|^2}{|69.79 + 9.98\alpha|^2}$$

Efectivament, la relació d'intensitats disminueix amb el grau d'ocupació (amb la relaxació de vacants). Això queda mostrat a la figura 11.

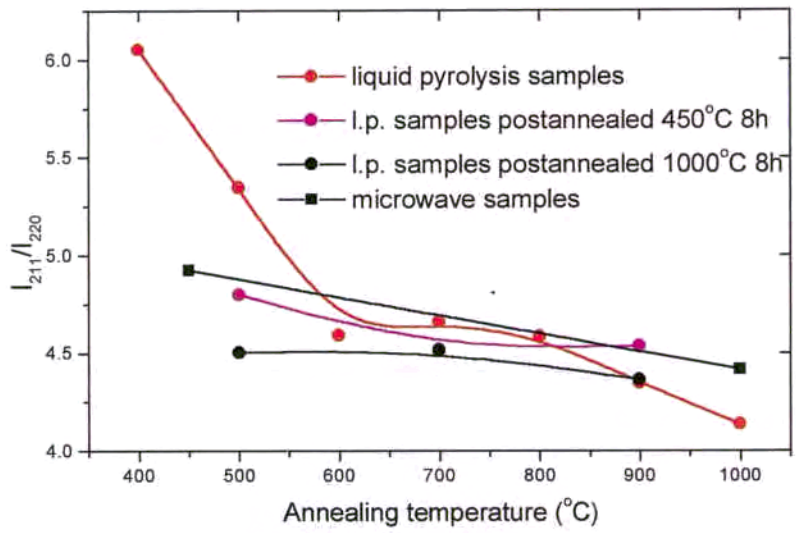

Figura 11. Relació d'intensitats (I_{211}/I_{220}) dels difractogrames de les mostres 5M (recuites i no) obtingudes per piròlisi líquida.

D'aquesta manera es confirma experimentalment que l'augment de la temperatura provoca un descens en la densitat de vacants d'oxigen, essent això la causa de diferències estructurals, alguna reflexada en posteriors resultats de XRD.

4.4 Verificació de la fiabilitat de les pols obtingudes per a aplicacions sensores: nanopols d'òxid d'estany obtingut per microones en substractes micromecanitzats de silici

Com a resultat d'aquestes noves tecnologies es possible obtenir sensors d'altes prestacions i baix consum. A tall d'exemple es presenten les característiques de sensors d'òxid d'estany modificats amb diferents concentracions de pal·ladi –figura 11-. Mentre una baixa concentració de pal·ladi permet obtenir una bona selectivitat a CO, una addició superior n'elimina aquesta component i permet captar exclusivament metà.

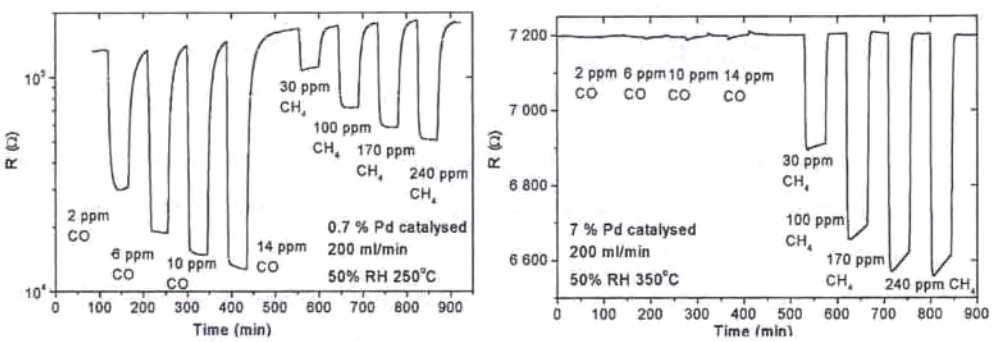

Figura 5. Resposta dinàmica dels sensors de SnO_2 modificats amb pal·ladi en diferents proporcions. S'aprecia com mentre, a l'esquerra, una catalització baixa en pal·ladi dóna una

Aquest tipus de resposta permet establir un algorisme pel càlcul de concentracions que dóna uns extraordinaris resultats fins i tot quan el sensor es sotmès a barreges binàries. Com es pot apreciar a la taula 4.

D'aquesta manera queda garantida la fiabilitat dels sensors presentats, que mantenen les característiques de sensitivitat, selectivitat, estabilitat i consum intel·ligent.

Concentratió Real		Concentratió predita	
CO (ppm)	CH_4 (ppm)	CO (ppm)	CH_4 (ppm)
200	200	189.0 (5.5%)	177.8 (11.1%)
400	400	402.5 (0.6%)	384.7 (3.8%)
100	4000	92.0 (8%)	4116.9 (2.9%)

Taula 4. Concentracions reals i predites de CO i CH_4 utilitzant l'algorisme de càlcul de concentracions en barreges binàries. Entre parèntesi hi ha l'error relatiu.

5. Caracterització aplicada a sensors de capa primas

5.1 Introducció

En aquest darrer capítol s'estudien mostres obtingudes per pulverització catòdica (sputtering) atenent a la importància científica i tecnològica que ha tingut aquesta tecnologia en els darrers temps.

Els grups de mostres estudiats són els presentats a la taula 5. La principal variació consisteix en el blanc utilitzat i en la composició atmosfèrica en la que les mostres són crescudes. Finalment també s'analitza la influència un flash posterior de paladi per a catalitzar les mostres.

Grup	**1**	**2**	**3**
Composició del blanc	SnO_2	Sn	Sn
Atmosfera de cambra	70%Ar+30%O_2	100%O_2	100%O_2
Catalització	No	No	Posterior flash Pd

Taula 5. Conjunts de mostres estudiades en aquest apartat.

5.2 Evolució microstructural de l'òxid d'estany nanocristal·lí en capa prima

Mitjançant l'estudi per diffracció de rajos X (XRD) i espectroscòpis de fotoelectrons (XPS) analitzem el conjunt de mostres descrit.

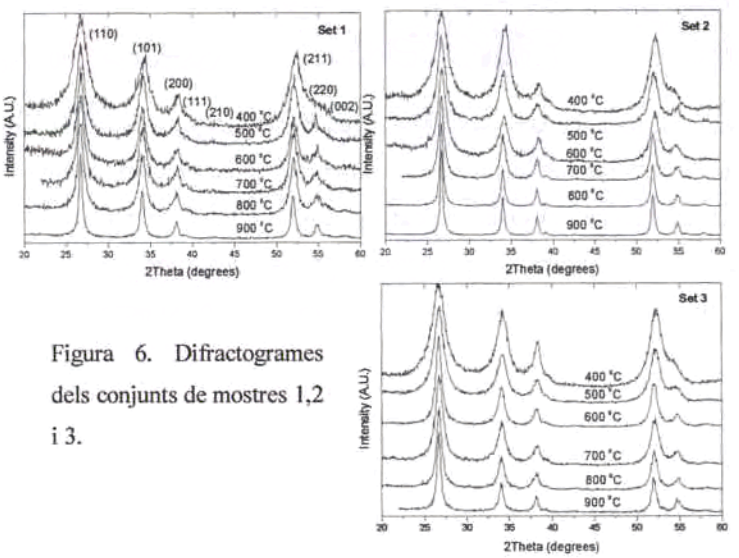

Figura 6. Difractogrames dels conjunts de mostres 1,2 i 3.

Com es pot apreciar en la figura 6, l'estudi de l'evolució dels patrons de difracció revela una clara tendència a la cristal·linitat quan s'augmenta la temperatura de recuit. Una anàlisi més acurada d'aquests efectes mostra com hi ha un conjunt de distorsions associades a aquests efectes. A la taula 6 es mostra com la distància interatòmica que presenten aquestes mostres és inferior a la catalogada (dues darreres columnes) i per tant aquestes mostres pateixen distorsions.

Reflection	$d_{hkl}^{900^\circ C}$ (Å)	$d_{hkl}^{900^\circ C}$ (Å)	$d_{hkl}^{900^\circ C}$ (Å)	$d_{hkl}^{1000^\circ C}$ (Å)	d_{hkl} (Å)
	Set 1	**Set 2**	**Set 3**		
(110)	3.337	3.340	3.338	3.351	3.347
(101)	2.634	2.636	2.634	2.637	2.643
(211)	1.760	1.761	1.760	1.762	1.764
(220)	1.674	1.673	1.674	1.672	1.675

Taula 6. Distància entre plànols atòmics calculada mitjançant la fòrmula de Bragg. A les dues darreres columnes hi ha una referència de valors trobats a la literatura.

Un estudi exhaustiu de la resta d'efectes relacionats amb les dades de XRD així com el resultats de XPS permet identificar la compacticitat de les capes primes com el causant d'aquest efecte. No obstant, la similar evolució que presenten les mostres amb comparació a les estudiades prèviament permet identificar que l'esmentat efecte és competitiu amb l'evolució de vacants d'oxigen amb la temperatura de recuit.

5.3 Estudi de les estratègies de catalització de l'òxid d'estany en capa prima

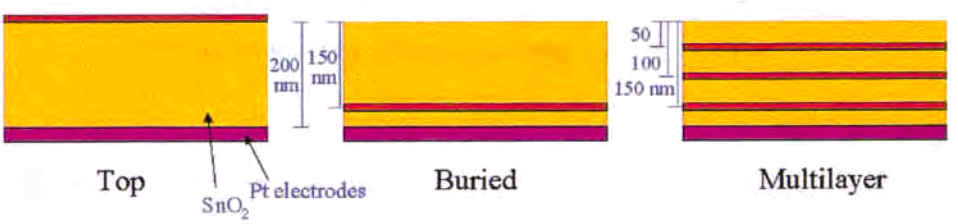

Figura 7. Diferents estratègies de catalització de les capes primes d'òxid d'estany.

Per a millorar les propietats sensors de les capes primes d'òxid d'estany es procedeix a l'estudi de les estratègies de catalització. Per a aquest motiu s'utilitzen paladi i platí com a agents catalitzadors.

La seva implementació es realitza mitjançant el dipòsit per pulverització de capes de catalític. Així, la disposició del conjunt dóna lloc a les diferents configuaracions estudiades. En el cas de la catalització superior (top), el catalític es situa a la part superior de l'òxid d'estany. Una altra aproximació és utilitzar una capa catalítica enterrada (buried). Finalment, quan diverses capes són enterrades, obtenim una disposició multicapa (multilayer). Veure figura 7.

L'estudi mitjançant XPS dels perfils de profunditat de les mostres, revela una capacitat de difussió pel paladi, mentre que el platí té una avidesa per a formar clústers. Aquesta situació dona lloc a que les catalitzacions superiors siguin poc eficaces, ja que en el cas

del paladi es dificulta la penetració del gas a estudiar en la capa sensora. En el cas del platí, els clusters esdevenen catalíticament inactius.

Igualment la catalització multicapa esdevé excesiva, ja que en afegir-hi diverses dosis del material catalític, la difusió d'aquest provoca que hi hagi zones amb una altísima concentració de catalitzador.

Resultats molt més interesants s'obtenen amb la catalització enterrada. Especialment en el cas del platí, en que es registren notables augments de la sensitivitat al CO.

6. Conclusions, principals troballes i revisió crítica

Com a principals troballes podem esmentar:

- ✓ l'obtenció de pols de SnO_2 nanocristal·lí com mitjançant la nova tecnologia de piròlisi líquida i la seva caracterització
- ✓ l'obtenció de pols de SnO_2 nanocristal·lí com mitjançant la nova tecnologia de tractament de microones i la seva caracterització
- ✓ el disseny i posta a punt d'una tècnica (microimpresió) per la implementació d'òxid d'estany en substractes micromecanitzats de silici
- ✓ el disseny d'una nova tècnica (recobriment per pulverització) per a la implementació massiva de SnO_2 en substractes micromecanitzats de silici
- ✓ la realització d'un estudi de caracterització del material sensor obtening l'evolució nanostructural en funció de la temperatura de recuit
- ✓ la utilització satisfactoria d'òxid d'estany nanocristal·lí amb propietats de filtre catalític per a la mesura selectiva de barreges binàries CO/CH_4
- ✓ el desenvolupament d'un algorisme, que bassat en l'anterior efecte, quantifica la proporció d'aquests gasos

Com a principals inconvenients d'aquest estudi en podem citar la manca d'estudi a llarga termini dels sensors implementats i la manca de mesures elèctriques de les mostres que han permes elaborar l'estudi de l'evolució nanostructural en funció de la temperatura de recuit.

Amb els presents resultats, creiem que s'aporta un contingut novedós en el camp dels sensors de gas semiconductors basats en òxid d'estany nanocristal·lí, que permet el seu desenvolupament mantenint sensitivitat, selectivitat, estabilitat i baix consum.